

Open-Source Parametric Airfoils to Study Geometric Effects on Buffet

Zauner M.^{*}, Lusher D. J.[†], Moise P.[‡], Sansica A.[§], Hashimoto A.[¶], and Sandham N. D.^{||}.
Japan Aerospace Exploration Agency, Chofu, Tokyo, 182-8522 Japan
University of Southampton, Southampton, Hampshire, SO17 1BJ, UK

Recent research into buffet in the transonic flow regime has been focused on a limited number of proprietary airfoil geometries and has mainly considered parametric variations in Mach number and angle of attack. In contrast, relatively little is known about the sensitivity of buffet frequencies and amplitudes to geometric properties of airfoils. In the present contribution, an airfoil geometry construction method based on a small number of parameters is developed. The resulting airfoils and computational grids are high-order continuous everywhere except at the trailing edge corners. The effects of four key geometric parameters, defined by local extrema of coordinates on the airfoil at the design condition and denoted as ‘crest’ points, are studied using large-eddy simulation, considering both free-transitional and tripped boundary layers. For both states of the boundary layer, buffet amplitude and frequency are found to be highly sensitive to the axial and vertical position of the suction-side crest point, while the vertical crest position on the pressure side affects the mean lift. The present work confirms that buffet can appear for free-transitional (laminar buffet) and tripped conditions (turbulent buffet) with similar sensitivities. For test cases near onset conditions intermediate-frequency phenomena have been observed, which were linked to unsteadiness of separation bubbles. Frequencies scaling based on mean-flow properties of the separation bubble were shown to be in good agreement with previous findings on different airfoil geometries in Zauner *et al.* (Flow Turb. & Comb., Vol. 110, 2023, pp. 1023-1057). Airfoil geometries are provided as open source: <https://doi.org/10.5281/zenodo.12204411>.

I. Introduction

The safe flight envelope of aircraft is typically limited by an unsteady flow phenomenon called “buffet”, leading to strong vibrations of wings and control surfaces. Buffet can be categorised according to the speed regime (i.e. low- and high-speed buffet), spatial properties (i.e. extruded two-dimensional geometry invariant in the spanwise direction, swept profiles, and fully three-dimensional wing configurations), and airfoil properties (i.e. symmetric and asymmetric). Buffet research in literature has a strong focus on high-speed applications, where compressibility effects cannot be ignored, and is often referred to as ‘transonic buffet’. A possible connection between low- and high-speed buffet is still under investigation and discussion [1, 2], but the focus of the current work lies on transonic buffet. Transonic buffet has been linked to linear instabilities observed within a narrow band before stall for two-dimensional airfoils, swept wings [3], as well as fully three-dimensional aircraft configurations [4, 5]. Even though two-dimensional buffet phenomena can co-exist for swept wings [6] as well as half-wing-body configurations [7, 8], three-dimensional phenomena like buffet cells [9], which have been shown to be essentially stall cells [1], are also likely to be present and often dominate the flow dynamics. Even for unswept infinite wings, Lusher *et al.* [10] identified both 2D shock-oscillation and 3D buffet-cell modes at different frequencies, applying high-fidelity methods and aspect ratios of up to $AR = 3$. Here, we focus on buffet over unswept wing sections on a narrow domain, exhibiting so-called ‘two-dimensional buffet’. Furthermore, we consider only supercritical airfoil profiles exhibiting Type II buffet [11], (for which shock waves are present and oscillate only on the suction side). We investigate laminar-flow profiles for free-transitional boundary layers, which are characterised by relatively flat suction-side surfaces and aim to delay the transition point as long as possible.

^{*}Researcher, Aviation Technology Directorate, Aircraft Lifecycle Innovation Hub, zauner.markus@jaxa.jp.

[†]Invited Researcher, Aviation Technology Directorate, Aircraft Lifecycle Innovation Hub, lusher.david@jaxa.jp.

[‡]Visitor, University of Southampton, p.moise@soton.ac.uk

[§]Researcher, Aviation Technology Directorate, Aircraft Lifecycle Innovation Hub, sansica.andrea@jaxa.jp.

[¶]Manager, Aviation Technology Directorate, Aircraft Lifecycle Innovation Hub, hashimoto.atsushi@jaxa.jp.

^{||}Professor, Aerodynamics and Flight Mechanics Group, University of Southampton, n.sandham@soton.ac.uk

Airfoil	Re	M	α	Transition	St_B	approx. $\Delta C_{L,max}$	X_U	Y_U	X_L	Y_L
V2C	500,000	0.7	4°	free	0.12	0.20	0.33	0.055	0.59	-0.095
V2C	500,000	0.735	4°	free	0.15	0.30				
OALT25	500,000	0.7	4°	free	0.035	< 0.05	0.26	0.044	0.54	-0.087
OALT25	500,000	0.735	4°	free	0.082	0.45				
OALT25	3,000,000	0.735	4°	free	0.082	0.10				
NACA0012	500,000	0.7	4°	free	–	–	0.18	0.043	0.53	-0.088
NACA0012	500,000	0.75	4°	free	0.12	0.4				

Table 1 Comparison of buffet characteristics of V2C, OALT25, and NACA0012 airfoils from simulation data reported in [14], [16], and [2], respectively. Crest-point coordinates of airfoil geometries at an angle of attack of $\alpha = 4^\circ$ are denoted by X_U and Y_U (suction side), as well as X_L and Y_L (pressure side).

For tripped boundary layers, we consider conventional supercritical airfoil shapes, which are similar to the popular OAT15A profile developed by ONERA.

Crouch et al. [12] showed that we can predict frequencies and onset conditions associated with transonic buffet using global stability analysis. However, we still do not fully understand the driving mechanism and how this mechanism depends on the shape of the airfoil. For different geometries, we often observe large differences in buffet frequencies, f_B , which are commonly normalised by the chord length, c and free-stream velocity, U_∞ (i.e., Strouhal number, here denoted as $St_B = f_B U_\infty / c$). Also, onset and offset conditions can vary significantly across different airfoil geometries. To set the scene for the present study, simulation results of Dassault Aviation’s V2C profile, ONERA’s OALT25 profile (both supercritical laminar-flow profiles), and the symmetric NACA0012 profile are shown in table 1 for a constant angle of attack of $\alpha = 4^\circ$ and free-transitional boundary layers. Besides Reynolds number (Re) and Mach number (M), also the angle of attack (α) and boundary-layer transition mode are listed. In addition, we provide the chord-based Strouhal numbers as well as approximate amplitudes of lift oscillations associated with buffet, denoted as St_B and $\Delta C_{L,max}$, respectively. We also list the location of so-called upper (X_U, Y_U) and lower (X_L, Y_L) crest points after rotating the profile by α , which will allow comparison with present parametric airfoil geometries and will be detailed later. Corresponding airfoil geometries at $\alpha = 0$ are illustrated in figure 1, including also a present OpenBuffet geometry with similar geometric properties as the V2C profile. At the design angle of $\alpha_D = 4^\circ$, the crest points of this profile will be located at $(X_U, Y_U) = (0.3, 0.06)$ and $(X_L, Y_L) = (0.6, 0.09)$, which will be discussed in more detail later. Considering moderate Reynolds numbers of $Re = 500,000$ at $M = 0.7$, Zauner et al. [13] and Moise et al. [14] reported Strouhal numbers of $St \approx 0.1$ for direct numerical and large-eddy simulations of the V2C profile, respectively, which agree well with wind-tunnel experiments by Placek and Ruchała [15] and Davidson2016a. Considering the OALT25 profile at the same α , M and Re , large-eddy simulations (LES) of Zauner et al. [16] show very weak low-frequency oscillations associated with incipient transonic buffet at much lower frequencies corresponding to $St_B \approx 0.035$. At an increase Mach number of $M = 0.735$, buffet frequencies for V2C and OALT25 profiles respectively increase to $St_B = 0.15$ and 0.082, but remain very different [16]. Despite significant geometric differences, LES of the symmetric NACA0012 by Moise et al. [2] show similar buffet frequencies compared to the V2C profile, while onset conditions differ.

Even though the mode of boundary-layer transition has significant impact on buffet onset conditions and amplitudes, frequencies seem to be less affected [17]. In their wind-tunnel experiments on ONERA’s OALT25 profile, Brion et al. [18] showed that low-frequency oscillations appear for tripped and free-transitional boundary layers at $St_B \approx 0.07$ and 0.05, respectively. For the latter test case, however, a co-existing intermediate-frequency phenomenon at $St_I \approx 1.1$ dominates the flow dynamics and has been associated with unsteadiness of the shock-induced separation bubble [16, 19]. Even though the buffet frequencies measured in experiments for the tripped OALT25 profile agree reasonably well with those of Jacquin et al. [20] reported for ONERA’s OAT15A ($St_B \approx 0.07$), we should bear in mind that flow conditions differ, as shown in table 2. Corresponding airfoil geometries are illustrated in figure 2, including also a present OpenBuffet geometry with similar geometric properties as the OAT15A profile (geometric details of the OB-3p5-2p8’4p8’3p8’7p8 geometry are specified in table 10 for test case OB-T-D2-4p9 and will be explained later).

In general, one could try to explain differences in buffet frequencies by acoustic feedback models similar to Roos [21] and Lee [22]. However, even though such models may match results for certain profiles under certain conditions for the OAT15A profile [23, 24], predictions of other studies did not agree with observations [14, 25, 26]. For the

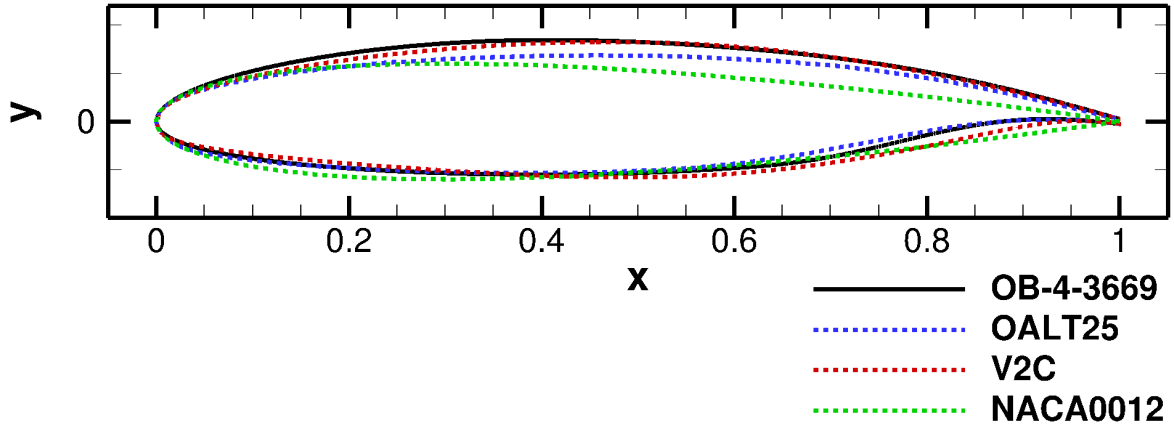


Fig. 1 Comparison of different laminar-flow airfoil geometries. The OB-4-3669 has its upper and lower crest positions at $X_U/Y_U = 0.3/0.06$ and $X_L/Y_L = 0.6/-0.09$, respectively.

Airfoil	Re	M	α	Transition	St_B	approx. PSD	X_U	Y_U	X_L	Y_L
OALT25[18]	3,000,000	0.735	4.0°	free	0.05	$4 \cdot 10^{-6} [p^2/q_0^2]$	0.26	0.044	0.54	-0.087
OALT25[18]	3,000,000	0.735	4.0°	tripped	0.07	$4 \cdot 10^{-4} [p^2/q_0^2]$				
OAT15A[20]	3,000,000	0.73	3.5°	tripped	0.07	$3 \cdot 10^{11} [p^2]$	0.25	0.048	0.37	-0.077

Table 2 Comparison of buffet characteristics of OALT25 and OAT15A airfoils. Cases at $Re = 3,000,000$ correspond to experimental data of [18] and [20]. The power-spectral density (PSD) measurements for OALT25 and OAT15A profiles are respectively based on pressure-sensor data at $x/c = 0.73$ and 0.45 .

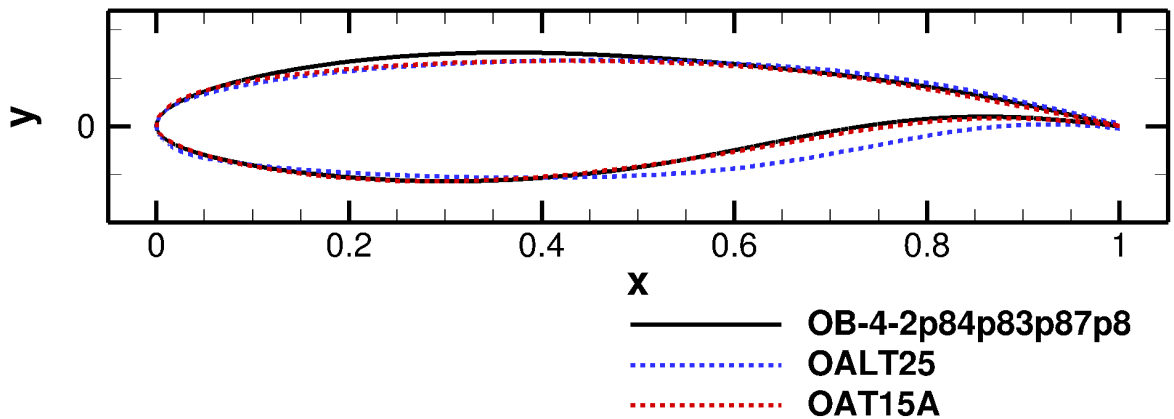


Fig. 2 Comparison of different conventional supercritical airfoil geometries. The OB-3p5-2p8'4p8'3p8'7p8 geometry is used for case OB-T-D2-4p8 and specified in table 10.

forementioned free-transitional test case, where freestream conditions are similar, buffet occurs for the OALT25 profile at almost four times lower frequencies compared to the V2C or NACA0012 profiles. Such significant variations are hard to explain by acoustic feedback models. Also for the example comparing tripped and free-transitional OALT25 experiments [18], significant variations of the shock position have been observed, while buffet frequencies remained similar.

On the other hand, geometric features of the airfoils are very likely to influence gradients in the flowfield and global stability characteristics. In tables 1 and 2, the coordinates of the crest points (the points denoting local extrema of the y -coordinate after rotation by α) are listed for the considered airfoil geometries. We can see that the upper crest is located further downstream for the V2C profile compared to the OALT25 airfoil (see also, Fig. 1). It also has an approximately 15% larger crest-to-crest thickness (the difference between the y -coordinates of upper and lower crest points after rotation by α). However, it is hard to interpret the significance of differences in crest-point locations with respect to transonic buffet. It is also interesting to note that main geometric differences between ONERA’s OALT25 and OAT15A profiles appear on the pressure side. However, based on results in literature it is impossible to conclude whether the good agreement of buffet frequencies for both airfoils is due to geometric similarities of the suction side profiles or mixed (competing) effects of variations of geometry and flow conditions. Despite the availability of extensive literature on experimental as well as numerical studies on transonic buffet, they are very often limited to single airfoil geometries. Given the fact that transonic buffet is highly sensitive to M , Re , α , and the mode of boundary-layer transition (free or tripped), results are often difficult to compare and it is hard to understand the isolated influence of geometric features on the dynamical behaviour of transonic buffet (i.e. onset, frequencies, amplitude, etc.).

In the present contribution, we want to analyse the sensitivity of buffet to geometric features such as crest-point locations for tripped and free-transitional boundary layers. Results can help us to learn more about the underlying buffet mechanism and provide insights into airfoil design, which poses significant challenges due to the high dimensionality of the geometry. Various parameterisation approaches have been adopted to simplify this design process to reduce the dimensionality of this problem. The set of parameters needs to be carefully chosen such that they allow for sufficient variation in the airfoil geometry, cause physically intuitive variations in the geometry, produce smooth profiles and have minimal redundancy. We can find a wide range of airfoil construction methods in the literature, which can be used for such parametric studies. Most of these methods aim to facilitate the conceptual design of new airfoils. Based on thin-airfoil theory, it is often beneficial to parametrise and optimise the camber and thickness separately to study a wide range of parameters, such as angles of attack and Mach numbers. The NACA airfoil series is a very popular example of this approach. Other methods, such as orthogonal basis function (OBF)[27] or class-shape function transformation (CST)[28, 29] methods, use polynomial functions to describe the shape of the airfoil contour, which facilitates the use of optimisation methods to analyse the aerodynamic performance for a wide range of flight conditions. For the present work, we are less interested in the airfoil performance or lift-drag polars. As we want to better understand the sensitivity of transonic buffet to geometric characteristics, we require increased control over the airfoil curvature at particular flow conditions, where buffet typically occurs. On the other hand, we want to keep the number of geometric input parameters as low as possible to facilitate the physical interpretations of results and trends, while maintaining a low number of cases and, consequently, minimising computational costs. In the context of using high-order discretisation schemes for high-fidelity CFD simulations, it is beneficial to describe the airfoil surface by high-order polynomials to avoid discontinuities in the metric terms. This is implemented in the present work, where the entire grid is generated by blending polynomial functions to guarantee continuous metric terms, where possible. The method developed is similar to the ‘Parametrised Section’ (PARSEC) method of Sobieczky [30], where an airfoil was defined by two sixth-order polynomials describing upper and lower sides. For the PARSEC airfoils, position and curvature of upper and lower crest points, maximum and trailing-edge thickness, leading-edge radius, and trailing-edge angles at zero incidence, sum up to a total of 11 parameters, but we emphasise that their focus was not on transonic buffet. We should keep in mind that when we design or parametrise an airfoil at zero inclination, airfoil properties like crest locations change with the angle of attack. While effect of chord-rotation or camber on aerodynamic mean properties can be explained by the thin-airfoil theory, the effects of variations of crest points and the projected airfoil thickness (or crest-to-crest thickness) are more difficult to predict.

In the current approach, segments between the leading edge and crest points on either side of the airfoil are described by blended ellipses, whilst sixth-order polynomials are used to connect the crest points to the trailing edge. In contrast to the PARSEC method, we define these parameters at a specified design angle α_D , where we expect buffet to occur. Parameters (e.g. crest-point locations) can then be varied about this point without the need to consider rotation transforms at a given angle of attack. The angles at the trailing-edge corners (‘trailing-edge angle’ and ‘boat-tail angle’ correspond to upper and lower corners of the trailing edge, respectively) are here defined with respect to the horizontal

axis at the design angle. Considering also trailing-edge thickness leaves us with a total of 10 parameters to describe the present ‘OpenBuffet’ (OB) airfoil geometries, which are listed in table 3 together with those of the PARSEC method. More details about the airfoil construction method will be provided in the Methodology section. Compared to the PARSEC airfoils, the present approach is more intuitive, as it does not require the specification of derivatives. This makes it also straight forward to mimic existing airfoils, as crest points are easier to measure than derivatives. We want to re-emphasise at this point that this study does not aim to replicate established airfoil geometries, for which better methods exist [31, 32]. Instead, our objective is to study geometric effects on unsteady flow phenomena at buffet conditions using a minimum set of intuitive design parameters. In order to reduce the parameter space for our current contribution, we set the semi-axes defining the leading-edge rounding to $a_{LE} = X_U$ and $b_{LE} = Y_U$, and fix the remaining parameters to obtain a four-digit airfoil series for a given design angle. The last column of table 3 contains an example of parameters of a representative parametric profile, which will be detailed in the next section.

Parameter	PARSEC	OpenBuffet	OB-4-3666
Design angle	0°	α_d	4°
Upper crest streamwise position	X_U	$X_U = D_1/10$	0.3
Upper crest vertical position	Y_U	$Y_U = D_2/100$	0.06
Lower crest streamwise position	X_L	$X_L = D_3/10$	0.6
Lower crest vertical position	Y_L	$Y_L = -D_4/100$	-0.06
Leading-edge rounding	Upper leading-edge radius r_U	Semi-major axis of ellipse a_{LE}	X_U
	Lower leading-edge radius r_L	Semi-minor axis of ellipse b_{LE}	Y_U
Trailing-edge angle	α_{TE}	$\alpha_{TE} = D_5/10$	20°
Boat-tail angle	β_{TE}	$\beta_{TE} = D_6/10$	10°
Trailing-edge thickness	Δ_{TE}	$\Delta_{TE} = D_7/1000$	0.005
Upper crest curvature	$Y''_u(x = X_U)$	N/A	N/A
Lower crest curvature	$Y''_l(x = X_L)$	N/A	N/A

Table 3 Comparison between parameters of present OpenBuffet airfoils and PARSEC airfoil geometries.

In summary, this study aims to shed light on the effect of geometry on transonic buffet, by formulating parametric airfoil profiles that allow for a systematic variation of certain key geometrical features at a given angle of attack. To reduce the parameter space, we focus on the coordinates of upper and lower crest points provided by a four-digit airfoil series. Airfoil geometries have been made openly available (<https://doi.org/10.5281/zenodo.12204411>).

In the following sections, we will first describe our simulation methods in §II.A & II.B and grid-generation §II.C, before detailing our proposed parametric airfoil geometries in §II.D. We then show results for these parametric airfoil geometries, investigating the influence of the upper crest location in §III, where free-transitional as well as tripped boundary layers are considered in §III.A and §III.B, respectively. To extend the parameter space, additional simulations for free-transitional boundary layers are shown in §IV for modified airfoil geometries, including also analysis of the lower crest locations. We will conclude this contribution in §V.

II. Methodology

This work has been carried out in the scope of a collaboration between the Japanese Aerospace Exploration Agency (JAXA) and the University of Southampton. Simulations considering free-transitional boundary layers have been carried out at the University of Southampton using their in-house code SBLI. For cases with tripped boundary layers, simulations were performed by JAXA using an open-source framework called OpenSBLI, which is able to leverage GPU architectures. Both numerical methods are described in the following sub sections.

A. Spectral-Error based Large-Eddy Simulations (SE-LES) used for free-transitional cases

For cases considering free-transitional boundary layers, we employ the in-house code SBLI [33] for scale-resolving numerical simulations. This code, extensively validated, has been utilised in various investigations, including studies

on shock-wave/boundary-layer interaction [34–36], subsonic wing sections [37, 38], and transonic buffet [17, 39, 40]. SBLI demonstrates robust performance in massively-parallelised simulations using structured multi-block grids across diverse high-performance computer architectures.

The compressible three-dimensional Navier-Stokes equations are normalised by the airfoil chord (c), freestream density (ρ_∞), streamwise velocity (U_∞), and temperature (T_∞). These equations are solved in non-dimensional form using fourth-order finite difference schemes (central at interior and the Carpenter scheme [41] at boundaries) for spatial discretisation. For temporal discretisation, we use a low-storage third-order Runge-Kutta scheme, and a total variation diminishing scheme is applied to capture shock wave features [42]. A non-dimensional time step of $\Delta t = 3.5 \times 10^{-5}$ Convective Time Units (CTUs) is maintained for all free-transitional simulations. For boundary conditions, zonal characteristic boundary conditions [43] are enforced at the outlet, while integral characteristic boundary conditions [44] are applied at the remaining outer boundaries.

In this contribution, we adopt a Spectral-Error based Implicit Large-Eddy Simulation (SE-ILES) scheme [40, 45]. This approach involves evaluating spectral error indicators [46] locally every $N_E = 30$ time steps corresponding to 0.00105 CTUs. These indicators control a sixth-order filter [47] to eliminate scales insufficiently resolved by the grid. Further details of this approach can be found in [48], where validation against DNS for a transonic buffet test case is also shown. Requirements for grid and domain independence, and the effect of various flow conditions (M , Re , α , transition type, *etc.*) have been examined using SBLI and reported in multiple studies [14, 16, 17, 40]. For the OALT25 profile, good agreement between simulation results of [16] and experimental measurements of [18] was found.

B. Implicit Large-Eddy Simulations using OpenSBLI for tripped turbulent cases

For simulations considering boundary-layer tripping, we use the multi-block OpenSBLI automatic code-generation framework for compressible CFD simulations [49, 50], developed at the University of Southampton and JAXA. OpenSBLI utilises symbolic algebra to automatically generate a complete finite-difference CFD solver in the Oxford Parallel Structured (OPS) [51] Domain-Specific Language (DSL). Users can define systems of partial differential equations to solve, which are expanded and discretized symbolically to create a simulation code tailored to the problem specified. The OPS library is embedded in C/C++ code, enabling massively-parallel execution of the code on a variety of high-performance-computing architectures via source-to-source translation, including GPUs. The OpenSBLI code was recently cross-validated against six other independently-developed flow solvers using a range of different numerical methodologies in [52] for a supersonic Taylor-Green vortex case involving shock-waves and transition to turbulence.

OpenSBLI applies high-order, non-dissipative central finite-differences to compute spatial derivatives, in cubic-split formulations to improve numerical stability [53]. Shock-capturing is performed by high-order Weighted Essentially Non-Oscillatory (WENO) schemes, applied in a characteristic-based filter framework [54]. For this study, fourth and fifth order schemes are used for central and WENO-based derivatives respectively. Grid metrics are computed with the same order of central scheme. A fourth-order one-sided boundary-closure [41] is applied at domain boundaries. A low-storage fourth-order explicit Runge-Kutta scheme is used for time-advancement, with a non-dimensional time-step of $\Delta t = 5 \times 10^{-5}$. An 11-point Dispersion-Relation-Preserving (DRP) explicit filter [55] is also applied to provide further stabilisation. To minimize the numerical dissipation introduced by the filter, a targeted filter approach (as described in [56]) is applied. A pressure-gradient-based sensor is computed to detect strong oscillations in the flow. The filter is applied only at these regions, and only at a frequency of once every 25 time-steps corresponding to 0.00125 CTUs. The airfoil surface is enforced by an isothermal no-slip boundary condition with wall temperature equal to the freestream value. Sponge zones are applied on the outer boundaries to maintain uniform freestream conditions. Data is written out from the solver every 0.05 CTUs to calculate the aerodynamic coefficients and flow visualisations.

Both high-fidelity codes (OpenSBLI and SBLI), have recently been cross-validated for a laminar buffet test case on the Dassault Aviation’s V2C profile at $Re = 500,000$ [56]. Excellent agreement was found for all aerodynamic coefficients and buffet quantities. Furthermore, OpenSBLI has been used to perform large-scale simulations of transonic buffet on turbulent wing profiles such as the NASA-CRM geometry in [10, 57]. In [57], OpenSBLI was cross-validated against results from URANS and global stability analysis obtained by JAXA’s unstructured solver FaSTAR [58], with excellent agreement found for buffet onset conditions, the main low-frequency buffet peak, and time-averaged aerodynamic quantities. In addition to sensitivity to numerical tripping strength, domain-width sensitivities were also examined for airfoils with span-widths equal to between 2.5% and 50% of chordwise length ($AR = 0.025 - 0.5$). In [10], OpenSBLI was applied to wide-span turbulent transonic buffet on aspect ratios of up to $AR = 3$. Three-dimensional buffet cells were identified with high-fidelity (ILES) methods for the first time. A Spectral Proper Orthogonal Decomposition (SPOD) method was applied to the data, identifying both 2D shock-oscillation and 3D buffet-cell modes. For the present

work on the influence of parametric airfoil geometries on buffet, an aspect ratio of $AR = 0.1$ is used as this was shown to provide domain-independent representations of trailing-edge separation for tripped cases in [57]. Further details of the open-source airfoil code used to perform the tripped cases in this work are given in [59].

To obtain turbulent conditions for this study, boundary-layer forcing is applied to trip the initially laminar boundary layer. The forcing is applied to the wall-normal velocity component near the leading edge, which is then used to set the momentum and total energy on the wall. Away from the forcing strip, the wall is a standard isothermal no-slip viscous boundary condition. The forcing is taken to be a modified form of the one given in [17] as

$$\rho v_w = \sum_{i=1}^3 A \exp\left(-\frac{(x-x_t)^2}{2\sigma^2}\right) \sin\left(\frac{k_i z}{0.05c}\right) \sin(\omega_i t + \Phi_i), \quad (1)$$

for simulation time t , trip amplitude $A = 0.075$, trip location $x_t = 0.07$, and Gaussian scaling factor $\sigma = 0.00833$. The three modes $(0, 1, 2)$ have spatial wavenumbers of $k_i = (6\pi, 8\pi, 8\pi)$, with phases $\Phi_i = (0, \pi, -\pi/2)$, and temporal frequencies of $\omega_i = (26, 88, 200)$. The effect of varied trip strength A , was investigated in [57]. Laminar, transitional, and fully-turbulent buffet interactions were identified based on the state of the boundary-layer upstream of the SBLI. The $A = 0.075$ level of tripping used in this study was shown in [57] to produce fully-turbulent buffet conditions as required. The other flow conditions for Reynolds, freestream Mach, and Prandtl numbers are taken to be $Re = 500,000$, $M_\infty = 0.73$, and $Pr = 0.71$. Sutherland’s law for dynamic viscosity is used with a reference freestream temperature of $T_\infty = 273.15K$.

C. Grid generation

The grids used in the present study have been generated using an open-source parametric grid-generation tool for high-fidelity grids called PolyGridWizZ and has been developed at the University of Southampton [60, 61]. We use 6th-order polynomials to define the geometry of grid lines and corresponding grid-point distributions. Such body-fitted grids are not necessarily limited to a single geometry, as grid lines are designed with respect to the position (coordinates) and local curvature with respect to the airfoil contour. Therefore, it is possible to use grids with very similar characteristics and resolutions for different airfoil geometries. For free-transitional cases, grids previously used for simulations of Dassault Aviation’s V2C profile and ONERA’s OALT25 airfoil and already assessed in terms of spatial resolution [61, 62] were adapted to the OpenBuffet parametric airfoil geometries. Tripped cases require finer grids to resolve the tripping location and breakdown to turbulence adequately. Grids for free-transitional and tripped cases consist of 75,350,600 and 346,720,500 points in total, respectively. Both grids consist of one C-type block and two H-type blocks, with details about resolutions shown in table 4. The number of grid points in circumferential and radial directions of the C-type block containing the airfoil are denoted by N_ξ and N_η , respectively. The two H-type blocks containing the wake region below and above the trailing edge of the airfoil are resolved by N_x and N_y grid points in freestream and perpendicular direction, respectively.

Transition type	Total grid count	C-block		H-block		L_z	N_z
		N_ξ	N_η	N_x	N_y		
Free-transitional	75,350,600	1495	480	799	494	0.05	50
Tripped	346,720,500	2251	630	709	630	0.1	150

Table 4 Grid resolutions of free-transitional and tripped LES grids.

D. OpenBuffet parametric airfoil geometries (“OB”)

The OpenBuffet parametric airfoil geometries are composed of elliptical shapes connecting the leading edge with local extreme points on both the upper and lower sides of the airfoil. These specific locations, indicative of crests, will be henceforth referred to as ‘crest points’. To connect the crest points with the trailing edge, we use 6th-order polynomials.

The shape of an ellipse is, generally speaking, more intuitive compared to high-order polynomials and is defined by

only two parameters denoted by their semi-axes according to

$$x_e = a_e \cos(\psi) + x_0, \quad (2)$$

$$y_e = b_e \sin(\psi), \quad (3)$$

where ψ is linearly discretised by N_ψ points ranging from $\pi \geq \psi \geq \pi/2$. In the present context, ellipses are always centered around $y_0 = 0$, while the x -location of the center (x_0) can vary. The discretisation of the profile (*i.e.* N_ψ) needs to be sufficiently higher than the wall resolution of the final CFD grid. For the present cases, where the entire airfoil surfaces is resolved by $N_{xi} \approx 1,500$ points in the circumferential direction using a minimum spacing of $\Delta s = 0.0003$, we chose 100,000 points to describe the raw geometry (High resolutions are favourable for accurate computation of gradients and interpolation of polynomial grid-distribution functions). The coordinates of the crest points (*i.e.* the endpoints of the ellipses) are defined at a design angle of attack α_D . This allows us to directly parameterise the crest points at an angle of attack of interest (*e.g.*, where buffet occurs), without accounting for rotation transforms. The full name-tag of OpenBuffet parametric airfoils is composed of 10 parameters according to the second column of table 3: OB- α_D - D_1 D_2 D_3 D_4 - a_{LE} b_{LE} - α_{TE} β_{TE} - Δ_{TE} (if applicable, the decimal point of parameters is replaced by the letter ‘p’). We will briefly introduce the parameters of the name tag referring to figure 3(c), while remaining details of this figure will follow below. The design angle α_D is marked green and denotes the rotation of the chord, while the upper and lower crest points defined by digits $D_1 - D_4$ are labeled by their respective coordinates (X_U, Y_U) and (X_L, Y_L) in blue. Angles α_{TE} and β_{TE} , defining the angles at the corner of the blunt trailing edge are labeled orange and cyan, respectively. The trailing-edge thickness Δ_{TE} denotes the distance between upper and lower trailing-edge corners.

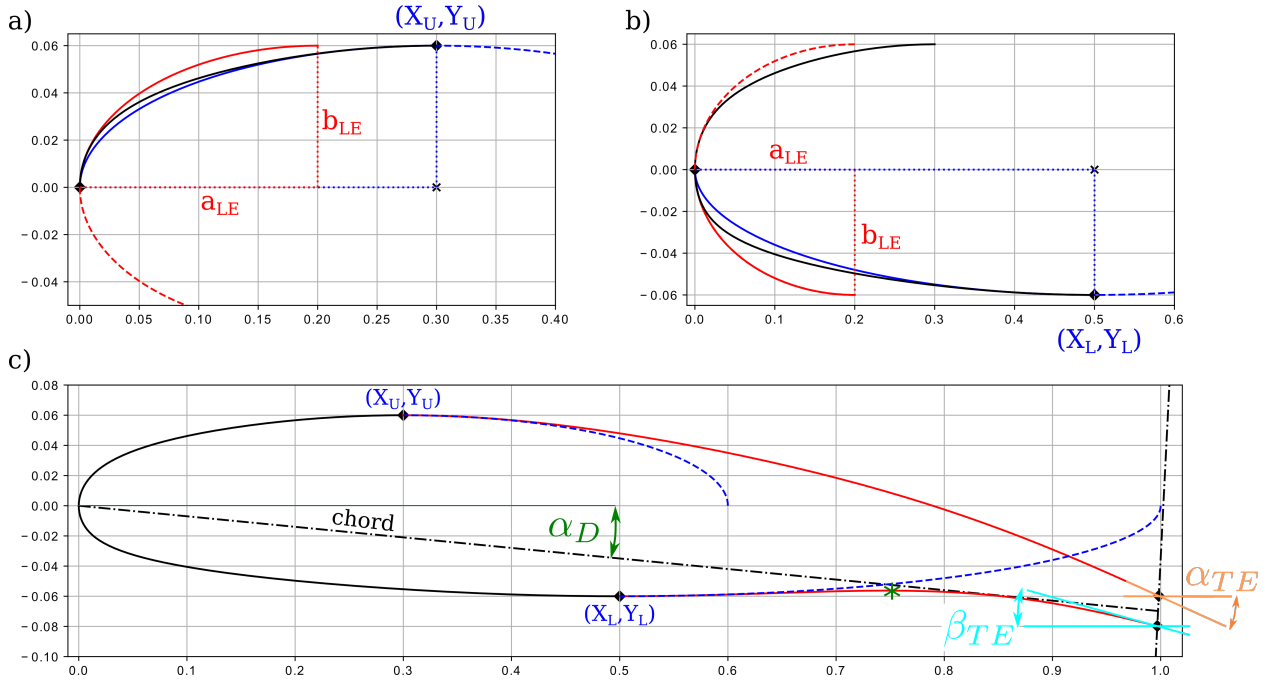


Fig. 3 Sketch of an OB-4-3656-26-1p81-5 profile: (a) and (b) show the construction of the leading edge, while (c) shows (in red) the polynomials connecting to the trailing edge and (in blue dashed lines) the semi-ellipses used in the construction.

The construction of OpenBuffet airfoil geometries is done in four main steps, with figure 3 providing visual aids for clarity. The aspect ratio between x and y coordinates is intentionally distorted in the figure to emphasize geometric features. The (x, y) coordinates for the leading edge, $(0, 0)$, upper and lower crest, (X_U, Y_U) and (X_L, Y_L) , respectively, are defined *a priori* for a given airfoil. The first four digits of the airfoil, D_1 to D_4 , can be used to calculate (X_U, Y_U) and (X_L, Y_L) , as given in table 3. Strictly speaking, there are two crest points denoting local extrema on the lower side. The crest point, we control is usually the convex one (denoted by the black diamond symbol) upstream of the inflection point, where the second derivative switches sign. The second concave crest point is denoted by the green symbol. Increasing Y_L , the inflection point moves upstream and coincides at a certain value with the crest point we are controlling. When

further increasing Y_L , the inflection point moves further upstream and, eventually, we control the concave crest. This is, for example, the case for the OB-4-3663 airfoil. The curves connecting the leading edge and the crest points (*i.e.* the fore part of the airfoil) are determined by three ellipses. The first ellipse (shown in red in figure 3(a) and (b)) is used to define the leading edge curvature and is common for both the upper and lower surfaces according to

$$(x - a_{LE})^2/a_{LE}^2 + y^2/b_{LE}^2 = 1. \quad (4)$$

The other two ellipses are used to match the coordinates of the upper and lower crest points (shown in blue in figure 3(a) and (b)) and can be expressed as:

$$(x - X_U)^2/X_U^2 + y^2/Y_U^2 = 1 \quad (5)$$

$$(x - X_L)^2/X_L^2 + y^2/Y_L^2 = 1 \quad (6)$$

To ensure a smooth transition from the first ellipse to the other two on each side, a blending function is used. This blending function, $f(i)$ with $1 \leq i \leq N_\psi$, ranges from $f(1) = 1$ to $f(N_\psi) = 0$ and can be defined by a 6th-order polynomial

$$f(i) = Ai^6 + Bi^5 + Ci^4 + Di^3 + Ei^2 + Fi + G. \quad (7)$$

Higher derivatives at the bounds are set to zero ($f'(1) = f''(1) = 0$ and $f'(N_\psi) = f''(N_\psi) = f'''(N_\psi) = 0$). The additional third derivative at the starting point (leading edge) delays the transition from the leading-edge ellipse to the ellipse defined by the crest point. The smooth transition from the red ellipse at the leading edge to the blue one at the crest point is demonstrated in figures 3(a), where the resulting blended black curve is discretised according to:

$$x_0(i) = X_U - f(i)(X_U - a_{LE}) \quad (8)$$

$$a_e(i) = X_U - f(i)(X_U - a_{LE}) \quad (9)$$

$$b_e(i) = Y_U - f(i)(Y_U - b_{LE}), \quad (10)$$

which can then be substituted into equations 2 and 3 to obtain corresponding coordinates. Note that semi-axes as well as origin of the blended ellipse are now functions of ψ (discretised by i), where $i = 1$ recovers the leading-edge ellipse, while $i = N_\psi$ corresponds to the ellipse spanned by the crest point. The same procedure is performed on the lower side as shown in figure 3(b). Before connecting the crest points with the corners of the trailing edge, we rotate the chord by the design angle α_D , *i.e.*, $(\cos \alpha_D, -\sin \alpha_D)$. The rotated chord is depicted by a black dash-dotted curve in figure 3(c), where the corners of the trailing edge are located (orthogonal to the rotated chord) at a distance of $\pm \Delta_{TE}/2$. Having determined the starting and ending points, we can now define 6th-order polynomials $P(i)$ (with $1 < i \leq N_\psi$) to connect the crest points with the corners at the trailing edge. The derivatives at the crest points need to match those of the ellipse (*i.e.* $P'(1) = 0$ and $P''(1) = -b_e(N_\psi)/(a_e(N_\psi)^2$). At the trailing edge, first-order derivatives are given by trailing-edge and boat-tail angles α_{TE} and β_{TE} (with respect to the x axis), respectively. Both angles are shown in figure 3(c) and marked orange and cyan, respectively. Second- and third-order derivatives are set to zero. Polynomials for the upper and lower sides are denoted by red curves for the example in figure 3(c). After having obtained the full geometry at the design angle, we can rotate the coordinates back to zero degrees to obtain coordinates relative to the chord line in the usual convention.

For the 4-digit OpenBuffet airfoil series, we will limit the parameter space for a given design angle to four digits (D_1, D_2, D_3 and D_4): OB- α - $D_1D_2D_3D_4$. The semi-axes defining the leading-edge curvature are fixed as the coordinates of the upper crest (*i.e.* $a_e = X_U$ and $b_e = Y_U$). Thus, the leading edge-rounding on the upper and lower sides of the airfoil will change with the location of the upper crest points. While the forepart of the upper side is now defined by a single ellipse, there is still blending of two ellipses required on the pressure side. Parameters defining the trailing edge are similar to V2C and OALT25 geometries.

The baseline geometry for free-transitional cases of the present contribution corresponds to an OB-4-3666 profile, while we consider an OB-3p5-2p8'5p7'3p8'7p8 profile for tripped cases. The full set of parameters are listed in table 5. The latter OpenBuffet airfoil is defined by several parameters containing decimal numbers to obtain a geometry similar to ONERA's OAT15A profile, which ensures buffet at the given flow conditions. For clarity, we use the prime symbol ' to separate parameters $D_1 - D_4$ when we encounter multiple decimal number. We will also use name-tags for each test case in the parametric study, specifying only the parameters that differ from the reference geometry, instead of the lengthy airfoil definitions. Regarding Dassault Aviation's V2C geometry mentioned in the introduction, the geometric

Boundary layer	Angle of Attack	X_U	Y_U	X_L	Y_L	a_{LE}	b_{LE}	α_{TE}	β_{TE}	Δ_{TE}
Free-trans.	4°	0.30	0.060	0.60	-0.060	X_U	Y_U	18°	10°	0.005
Tripped	3.5°	0.28	0.057	0.38	-0.078	X_U	Y_U	17°	10°	0.000

Table 5 Parameters for baseline case with tripped and free-transitional boundary layers.

Label	Angle of Attack	X_U	Y_U	X_L	Y_L	a_{LE}	b_{LE}	α_{TE}	β_{TE}	Δ_{TE}
OB-F-Ref	4°	0.30	0.060	0.60	-0.060	X_U	Y_U	18°	10°	0.005
OB-F-D1-3p5	4°	0.35	0.060	0.60	-0.060	X_U	Y_U	18°	10°	0.005
OB-F-D1-4	4°	0.40	0.060	0.60	-0.060	X_U	Y_U	18°	10°	0.005
OB-F-D2-4p5	4°	0.30	0.045	0.60	-0.060	X_U	Y_U	18°	10°	0.005
OB-F-D2-4	4°	0.30	0.040	0.60	-0.060	X_U	Y_U	18°	10°	0.005

Table 6 Summary and labels for test cases considering free-transitional boundary layers.

features of the OB-4-3669 profile appear to be the most qualitatively similar. These geometries are shown in figure 1 together with ONERA’s OALT25 and the NACA0012 airfoils.

As already mentioned before, we consider in addition to the original OpenBuffet geometries (described in §II.D) a slight variation of the polynomial connecting crest points with the trailing edge. This leads to a flatter suction-side surface and increased robustness for extreme parameter choices as detailed in §IV.

III. Buffet Sensitivities to the Upper-Side Crest Position for OpenBuffet Airfoils

As discussed in the introduction, based on literature the upper-side geometry may have strong influence on buffet frequencies. Therefore, we want to investigate in the present section sensitivities of transonic buffet to the location (i.e. coordinates) of the upper crest point denoted by X_U and Y_U . In a first part we will assess test cases subjected to free-transitional boundary layers, using parametric OpenBuffet profiles that are similar to laminar-flow wing profiles like Dassault Aviation’s V2C profile. At such conditions, we typically observe full break-down to turbulence in vicinity of the shock location and relatively large shock-induced separation bubbles. In the second part we will then apply boundary-layer tripping to OpenBuffet profiles, which are similar to conventional supercritical airfoils like ONERA’s OAT15A geometry.

A. Free-transitional boundary layers

In this sub-section, we will study trends for aerodynamic properties and buffet characteristics for different airfoil shapes considering free-transitional boundary layers. Flow conditions are similar to previous studies of Moise et al. [14] and Zauner et al. [16] corresponding to $\alpha = 4^\circ$, $M = 0.7$, and $Re = 500,000$, where grid resolution and domain size requirements have been well established. Table 6 provides an overview of four-digit OpenBuffet geometries considered for this study. This airfoil family is representative of supercritical laminar-flow airfoils. For brevity, labels for test cases are composed of the profile name (‘OB’ for OpenBuffet), the transition mode (‘F’ for free-transitional), the digit (‘D1’ or ‘D2’) which differs from the reference case (OB-F-Ref), and the value of the latter.

1. Reference case OB-4-3666

As a reference test case we select the four-digit OB-4-3666 profile at $\alpha = 4^\circ$, $M = 0.7$ and $Re = 500,000$. Figure 4(a) shows the time- and span-averaged mean flow around this airfoil with free-transitional boundary layers. The red sonic line delineates the supersonic region with local Mach numbers larger than unity. The top plot of figure 4(b) shows respectively histories of lift and drag coefficients C_L and C_D . We observe large-scale oscillations associated with transonic buffet, where the lift coefficient (red curve: left-hand-side scale) leads the drag coefficient (blue curve: right-hand-side scale). Spectra of the bottom plot of figure 4(b) are computed using Fast Fourier Transform (FFT)

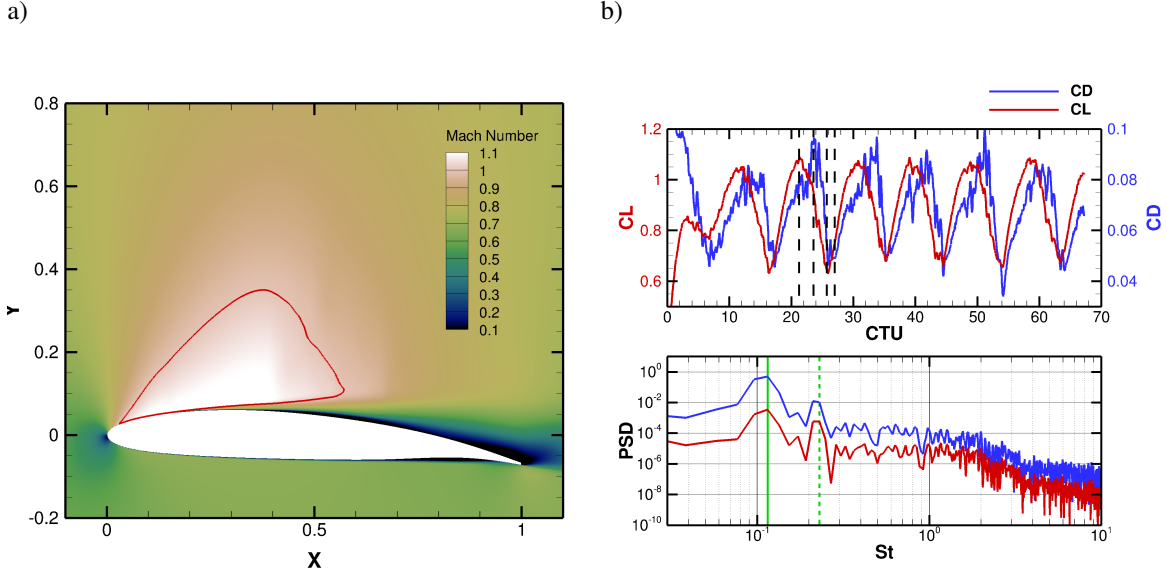


Fig. 4 (a) Time- and span-averaged flow field showing Mach number contours for the OB-4-3666 airfoil at $\alpha = 4^\circ$, considering free-transitional boundary layers, $M = 0.7$, and $Re = 500,000$. (b) Histories and spectra of lift (red) and drag coefficients (blue). Dashed lines mark time instances of snapshots in figure 6.

considering a single Hanning window and ignoring the initial transient of the first 15 convective time units (CTU), unless otherwise stated. The spectral resolution for the present time series corresponds to $\Delta St \approx 0.019$. We observe clear peaks for the buffet frequency corresponding to a Strouhal number of $St_B = 0.115$ and its harmonic at $St = 0.23$, which are respectively indicated by solid and dashed green lines. We will see later for different geometries where buffet is less dominant a secondary spectral peak arising at intermediate frequencies around $St \approx 0.5$ corresponding to a period of approximately 2 CTUs. Even though we do not observe such a clear peak in spectra of figure 4(b) for the baseline case, we can notice corresponding intermittent spikes in the C_D history during phases, where the drag is increased due to flow-separation phenomena (e.g. after 34 CTUs). To characterise buffet, we can measure maximum and minimum values of the lift coefficient ($C_{L,max}$ and $C_{L,min}$, respectively) as well as a maximum amplitude ($\Delta C_{L,max} = C_{L,max} - C_{L,min}$). For the reference case we obtain $\Delta C_{L,max} = 0.46$, $C_{L,max} = 1.09$, $C_{L,min} = 0.63$. We will use these as key parameters of interest for our parametric studies to characterise transonic buffet and its intensity.

Figure 5 shows time averaged (a) wall-pressure coefficient C_p and (b) skin-friction coefficient C_f distributions for the baseline profile for the free-transitional cases (underlying simulation data is sampled at time intervals of 0.035 CTUs at a 2D slice located at $z = 0$). The C_p reaches its maximum around $x \approx 0.3$. Due to the back and forth motion of the shock wave, the sharp pressure gradient across the shock wave appears as a smooth slope within the range of $0.30 < x < 0.65$ in the time-averaged flow field. Regions of $C_f < 0$ in figure 5(b) indicate laminar/transitional separation bubbles on the suction side in the range of $0.35 < x < 0.70$. While the mean flow re-attaches at $x \approx 0.7$, a secondary (turbulent) separation zone is observed near the suction-side trailing edge. While the mean flow on the pressure side remains attached near the trailing edge, we can observe a transitional separation bubble in the concave part around $0.7 < x < 0.9$. The inset of figure 5(b) provides a close-up of the re-attachment points for both sides.

Figure 6 shows numerical quasi-Schlieren snapshots (streamwise density gradient contours) at representative time instants indicated by vertical black dashed lines in figure 4(b). We will briefly outline the flow behaviour throughout one buffet cycle, while table 7 provides a summary of qualitative levels of aerodynamic coefficients with respect to their extrema at given time instances. Histories of corresponding coefficients are provided in figure 18(a) in appendix §V.A and will not be discussed here in detail. For a more in-depth analysis of transonic buffet at moderate Reynolds numbers and free-transitional boundary layers, we refer the reader to [14, 16]. Looking at figure 6(a), boundary layers are mostly attached on both sides of the airfoil, when the lift reaches its maximum. Towards the trailing edge, we observe flow structures originating from Kelvin-Helmholtz instabilities in the separating shear layer [63] and breaking down to turbulent vortices when passing through the shock wave [45]. The supersonic region approaches its maximum extent and is terminated by a normal shock wave. We observe multiple upstream-propagating pressure waves within the supersonic

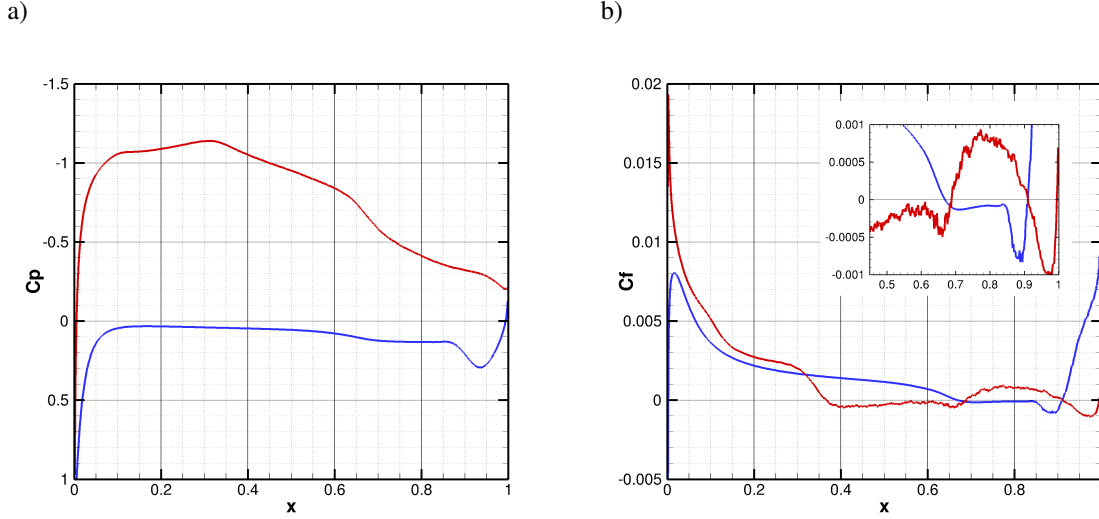


Fig. 5 Time-averaged (a) wall-pressure coefficient C_p and (b) skin-friction coefficient C_f distributions for the OB-4-3666 profile with free-transitional boundary-layers. Blue and red curves correspond to pressure and suction side distributions, respectively.

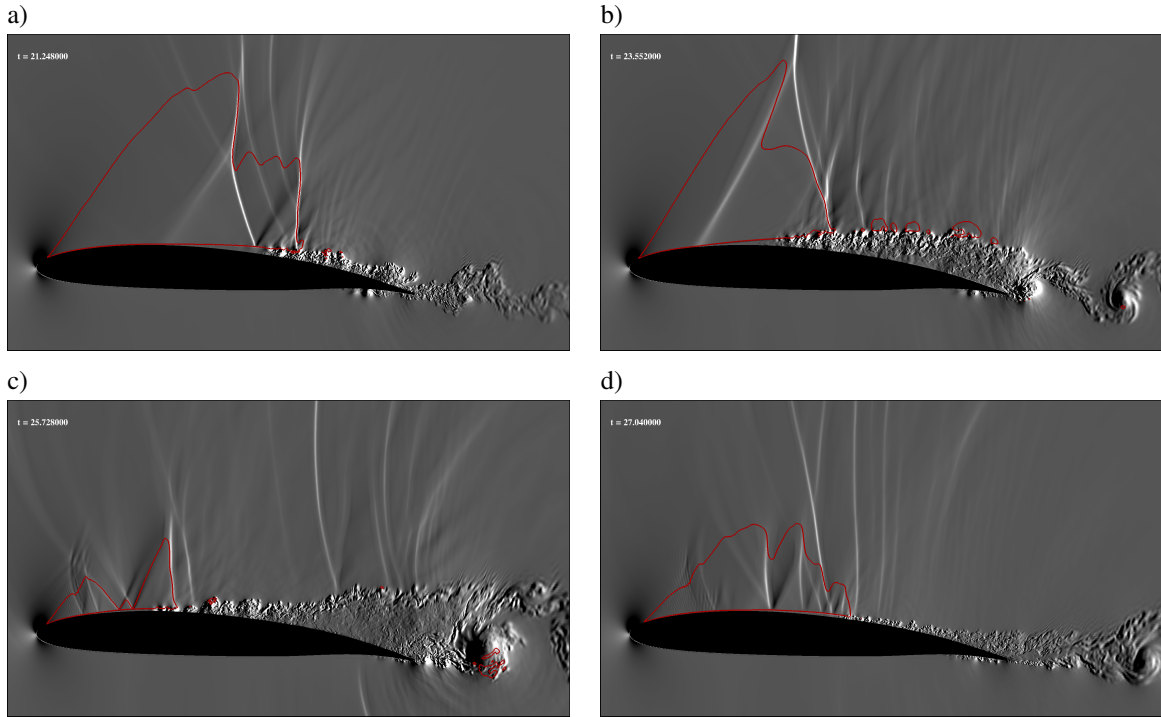


Fig. 6 Numerical quasi-schlieren snapshots showing streamwise density gradients after approximately (a) 21 CTUs (Convective time units), (b) 24 CTUs, (c) 26 CTUs, and (d) 27 CTUs, corresponding to vertical red lines in figure 4. Black and white contours correspond to non-dimensional values of $\partial\rho/\partial x = -5$ and 10, respectively. Sonic lines are shown in red.

region, which are introduced by acoustic waves circumventing this area. The present lambda-shock structure[16] and its dynamics look qualitatively very different from tripped cases or free-transitional cases at higher Reynolds numbers, but

Snapshot	time instant	C_L	$C_{D,p}$	$C_{D,f}$	C_L/C_D
a)	21.25	high	increased	medium	increased
b)	23.55	increased	high	low	low
c)	25.73	low	low	increased	reduced
d)	27.04	reduced	low	high	high

Table 7 Qualitative overview of aerodynamic properties for snapshots in figure 6.

are typical for present flow conditions [14]. Moving towards the next snapshot, flow separation develops and spreads rapidly upstream, leading to significant flow separation and shear layers diverging from the upper airfoil geometry. At the time instant in figure 6(b), the pressure drag reaches its maximum as aerodynamic forces are high and as a significant portion of the upper-side boundary layer is separated. This also leads to reduced skin-friction drag and lift-over-drag ratios. The separation wave of the lambda-shock structure strengthens and moves towards the leading edge. Strong vortical structures induce supersonic pockets above the shear layer and we can also see a well-pronounced vortex street in the wake behind the airfoil[14]. Eventually, the supersonic region degenerates into localised triangular pockets near the leading edge, as seen in figure 6(c), and the lift reduces. The airfoil is basically stalled at this time instant. At such conditions with reduced aerodynamic loads, the boundary layer can start recovering behind the shock foot and the re-attachment point starts moving downstream rapidly. This leads to a sharp increase in skin-friction, while the pressure drag grows at a much lower speed. We observe skin-friction reaching its maximum in figure 6(d), where the boundary layer is thin and fully attached. However, lift has barely increased at that time instant. While the flow is accelerating over the suction side recovering aerodynamic forces, we do not observe the formation of large Kelvin-Helmholtz structures.

The features seen here are the same as those seen for transonic buffet on the V2C, OALT25 and NACA0012 airfoils [2, 16, 17] under conditions of free transition and low to moderate Reynolds numbers. Furthermore, the periodic oscillations involving boundary layer separation and reattachment are the same as has been reported in other studies on transonic buffet at higher Reynolds numbers and forced transition (*e.g.* [9]). Thus, we conclude that the present parametric airfoil is capable of reproducing transonic buffet features adequately.

2. Horizontal variation of the upper crest point

Figure 7 shows simulation results for OpenBuffet geometries where the streamwise location of the upper crest point is varied (*i.e.* the first digit) between $0.3 \leq X_U \leq 0.4$ ($D_1 = 3.0, 3.5, 4.0$). While C_L histories are shown in figure 7(a), corresponding airfoil geometries are illustrated in (b). Note that the upper plot is distorted to make geometric differences clearer. Parameters selected to characterise aerodynamic properties and buffet characteristics are summarised in table 8. While buffet is clearly present in cases OB-4-3666 and OB-4-3p5666, the buffet amplitude decreases when delaying the crest point in the streamwise direction. Buffet frequencies, on the other hand, increase and additional peak arises at an intermediate frequency of $St_I \approx 0.3$, which appears to be similar to the separation-bubble mode reported in [16]. The reduction of buffet amplitudes, which is mainly due to increased levels of minimum lift, leads to an overall increase of the lift-over-drag ratio (\bar{L}/\bar{D}). For $X_U = 0.4$, the initial transient appears longer and we have to exclude the first 20 instead of 15 CTUs for spectral analysis. When moving from $X_U = 0.35$ to $X_U = 0.40$, we have to acknowledge a change in trends. As we can see in figure 7(b), the rear part of the red geometry becomes very steep, which promotes flow separation and some sort of post-buffet or stall conditions. While buffet seems to die out, oscillations at intermediate frequencies dominate the flow dynamics, while associated frequencies slightly increases from $St_I = 0.306$ to 0.338. We find mean-flow separation at $x \approx 0.55$, with no re-attachment up to the trailing edge and a significant divergence of the trailing-edge pressure. Mean C_p and C_f distributions can be found in appendix V.B. The mean C_L seems to settle near $C_{L,min}$ -levels of the OB-4-3p5666 case. We also observe frequencies around $St \approx 2$ associated with the wake mode reported by [14], which is typical for significant flow separation of the rear part. All these characteristics are typical for buffet-offset or stall conditions.

3. Vertical variation of the upper crest point

Figure 8 shows simulation results for airfoil geometries where the vertical location of the upper crest point is varied (*i.e.* second digit) between $0.04 \leq Y_U \leq 0.06$ ($D_4 = X = 4.0, 4.5, 6.0$), mainly affecting the airfoil thickness towards

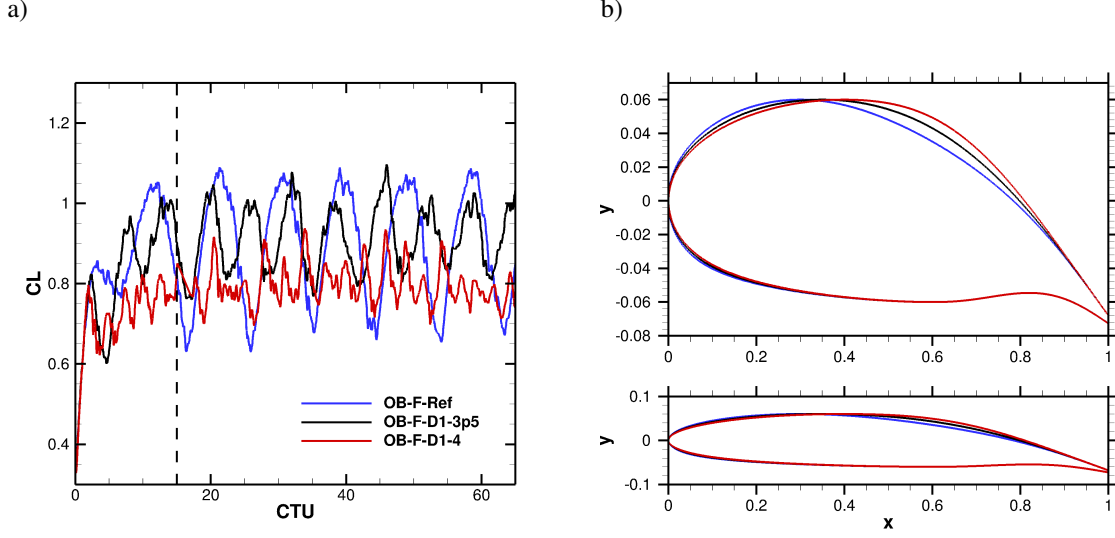


Fig. 7 (a) Lift coefficient (C_L) as a function of convective time units (CTU) for 4-digit airfoils at an angle of attack $\alpha = 4^\circ$, where the first digit is varied (OB-4-X666). Corresponding airfoil contours are shown in (b), respectively, where the aspect ratio of the upper plot axes is distorted. The aspect ratio of the lower plot is $x:y=1:1$.

Case	D_1	St_B	St_I	$\Delta C_{L,max}$	$C_{L,max}$	$C_{L,min}$	$C_{D,max}$	$C_{D,min}$	\bar{L}/\bar{D}
OB-F-Ref	3	0.115	-	0.46	1.09	0.63	0.102	0.039	12.4
OB-F-D1-3p5	3.5	0.153	0.306	0.34	1.1	0.76	0.102	0.036	14.3
OB-F-D1-4	4	-	0.338	0.25	0.94	0.69	0.104	0.048	11.1

Table 8 Summary of buffet characteristics for free-transitional cases varying the first digit of the reference case OB-F-Ref considering the OB-4-3666 profile.

the fore part as well as the rounding of the leading edge. Considering also table 9, we can observe buffet frequencies as well as corresponding amplitudes clearly increasing with Y_U . For cases with $Y_U < 0.06$, we see a spectral peak arising at intermediate frequencies in the range of $St_I \approx 0.5 - 0.6$. Decreasing Y_U delays buffet onset and improves the lift-over-drag ratio significantly. The observed increase of buffet frequencies with associated amplitudes agrees with the Mach-number study of [16] considering ONERA's OALT25 profile.

For test case OB-F-D2-4p5, we also applied a scaling for intermediate-frequency phenomena associated with an unsteady separation bubble proposed by [16]. We multiply the associated Strouhal number of $St_I = 0.573$ with the normalised mean length of the separation bubble $L_{sep}/c = 0.356$ and the maximum mean reverse velocity within the separation bubble $U_R/U_\infty = 0.102$. The obtained scaled Strouhal number of $St_R = 0.021$ agrees well with those reported in [16], ranging for different airfoils from $St_R = 0.20$ to 0.26 . Details about the meanflow data used for this scaling is provided in appendix V.D.

B. Tripped boundary layers

We will investigate in this sub-section parametric OpenBuffet profiles at tripped boundary-layer conditions to see, whether we can confirm certain observations and trends of free-transitional cases of the previous sub-section. While we aim for flow conditions similar to experiments of Jacquin et al. [20] corresponding to $\alpha = 3.5^\circ$ and $M = 0.73$, the Reynolds number is reduced to $Re = 500,000$, which also lowers computational costs and aligns with free-transitional computations of the previous section. Table 10 provides an overview of four-digit OpenBuffet geometries considered for this study. This airfoil family is representative of conventional supercritical airfoils, where case OB-T-D2-4p8

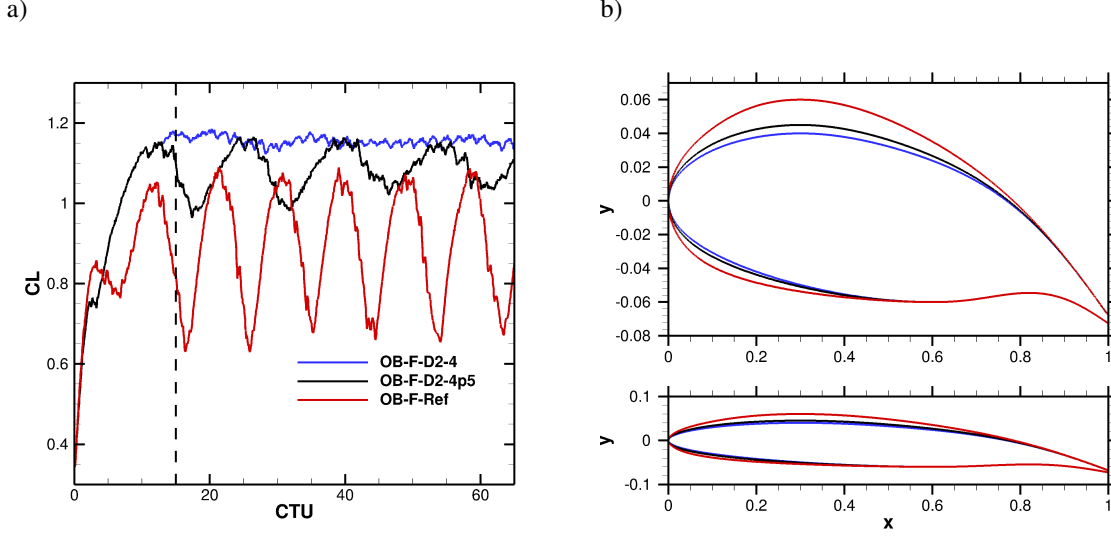


Fig. 8 (a) Lift coefficient (C_L) as a function of convective time units (CTU) for 4-digit airfoils at an angle of attack $\alpha = 4^\circ$, where the second digit is varied (OB-4-3X66). Corresponding airfoil contours are shown in (b), respectively, where the aspect ratio of the upper plot axes is distorted. The aspect ratio of the lower plot is $x:y=1:1$.

Case	D_2	St_B	St_I	$\Delta C_{L,max}$	$C_{L,max}$	$C_{L,min}$	$C_{D,max}$	$C_{D,min}$	\bar{L}/\bar{D}
OB-F-Ref	6	0.115	-	0.46	1.09	0.63	0.102	0.039	12.4
OB-F-D2-4p5	4.5	0.077	0.573	0.20	1.17	0.96	0.059	0.033	22.3
OB-F-D2-4	4	0.050	0.547	0.06	1.19	1.12	0.051	0.040	25.0

Table 9 Summary of buffet characteristics for free-transitional cases varying the second digit of the reference case OB-F-Ref considering the OB-4-3666 profile.

(OB-3p5-2p8'4p8'3p8'7p8) is similar to ONERA's OAT15A profile. Labels are composed of the profile name ('OB' for OpenBuffet), the transition mode ('T' for tripped), the digit ('D1' or 'D2') which differs from the reference case (OB-T-Ref), and the value of this digit.

1. Reference case OB-3p5-2p8'5p7'3p8'7p8

As a reference test case for tripped conditions, we select the four-digit OB-3p5-2p8'5p7'3p8'7p8 profile denoted as case OB-T-Ref. Figure 9(a) shows time- and span-averaged Mach-number contours at $\alpha = 3.5^\circ$, $M = 0.73$, and $Re = 500,000$. Compared to the free-transitional case, the supersonic region of the turbulent mean flow (delineated by the red curve) extends further into the free stream for the tripped case, where the shock foot is also much steeper. A weak kink in the sonic line at $x \approx 0.1$ is caused by an impinging wave originating from the tripping location. Figure 9(b) shows histories (upper plot) and spectra (lower plot) of lift (red curves) and drag coefficients (blue curves). Spectra are computed using FFT considering a single Hanning window and ignoring the initial transient of the first 20 convective time units (CTU). The spectral resolution for the present time series corresponds to $\Delta St \approx 0.013$. Similar to the free-transitional test case, we can observe a clear peak marked by the green solid line at $St_B \approx 0.09$, which is associated with transonic buffet. The harmonic peak is also visible and marked by the green dashed line at $St \approx 0.18$. Two additional peaks around $St \approx 6$ and 8 are caused by the forcing used to trip the boundary-layers.

Figure 10 shows time-averaged distributions of (a) wall-pressure coefficient C_p and (b) skin-friction coefficient C_f for the baseline profile. The boundary-layer tripping location is evident in both plots at $x = x_{tr} = 0.07$, but it is more pronounced in the skin-friction distribution, showing a spike on both sides. The C_p reaches its maximum around

Case	Angle of Attack	X_U	Y_U	X_L	Y_L	a_{LE}	b_{LE}	α_{TE}	β_{TE}	Δ_{TE}
OB-T-Ref	3.5°	0.28	0.057	0.38	-0.078	X_U	Y_U	17°	10°	0.000
OB-T-D1-3p0	3.5°	0.30	0.057	0.38	-0.078	X_U	Y_U	17°	10°	0.000
OB-T-D1-3p2	3.5°	0.32	0.057	0.38	-0.078	X_U	Y_U	17°	10°	0.000
OB-T-D2-4p8	3.5°	0.28	0.048	0.38	-0.078	X_U	Y_U	17°	10°	0.000
OB-T-D2-5p3	3.5°	0.28	0.053	0.38	-0.078	X_U	Y_U	17°	10°	0.000
OB-T-D2-6p1	3.5°	0.28	0.061	0.38	-0.078	X_U	Y_U	17°	10°	0.000

Table 10 Summary and labels for test cases considering tripped boundary layers.

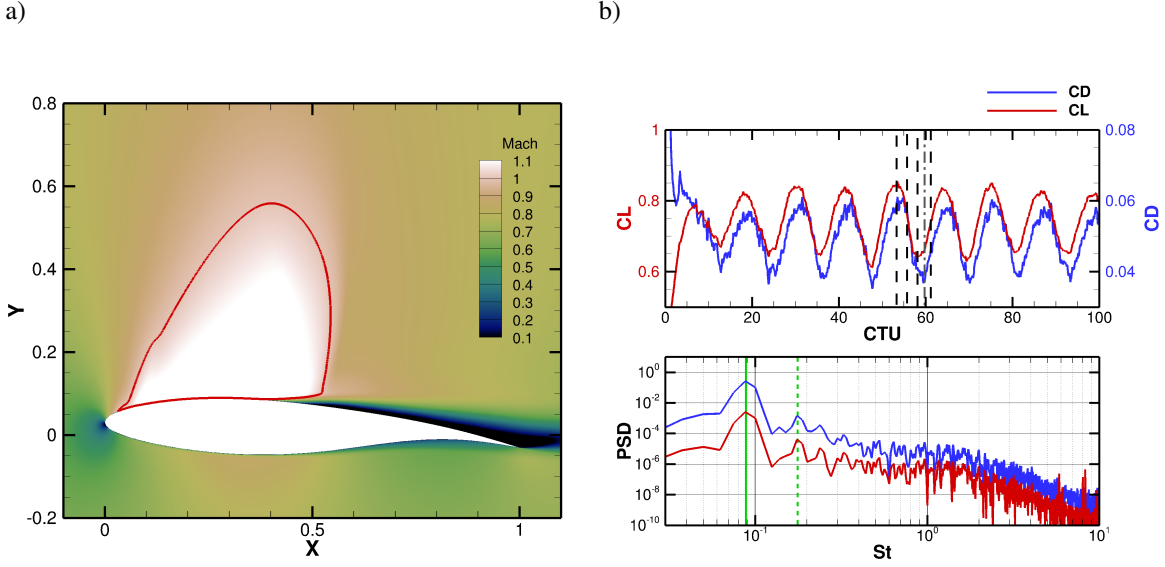


Fig. 9 (a) Time- and span-averaged flow field showing Mach number contours for the OB-3p5-2p8'5p7'3p8'7p8 airfoil at $\alpha = 3.5^\circ$, considering tripped boundary layers, $M = 0.73$, and $Re = 500,000$. (b) Histories and spectra of lift (red) and drag coefficients (blue). Dashed lines mark time instances of snapshots in figure 6

$x \approx 0.35$. Due to the back and forth motion of the shock wave, the sharp pressure gradient across the shock wave appears as a smooth slope within the range of $0.35 < x < 0.55$ in the time-averaged flow field. The same applies to the C_f distribution in figure 10(b), where the slope terminates with $C_f < 0$ indicating mean flow separation. While the mean flow re-attaches at $x \approx 0.75$ (see inset), we observe another mean-flow recirculation region near the trailing edge.

Figure 11 shows numerical quasi-schlieren snapshots (streamwise density gradient contours) at representative time instants indicated by vertical black dashed lines in figure 9(b). The vertical dash-dotted grey line marks an additional time-instant, which is qualitatively similar to figure 11(c) and will be included in the discussion. We will briefly outline the flow behaviour throughout one buffet cycle, while table 11 provides a summary of qualitative levels of aerodynamic coefficients with respect to their extrema. Histories of corresponding coefficients are provided in figure 18(b) in the appendix and will not be discussed in detail here. While we will outline main differences between tripped and free-transitional baseline cases, we refer the reader to [17, 18] for a more in-depth analysis of differences between transonic buffet subjected to tripped and free-transitional boundary layers. Starting at a high-lift phase, where C_L reaches its maximum in figure 11(a), we can observe a large supersonic region with its shock foot reaching the most down-stream location. Similar to the free-transitional case, we can observe a lambda-shock structure. However, due to the significantly smaller shock-induced separation bubble, the lambda-shock structure is much more localised for turbulent boundary layers and is reminiscent of experimental observations in [20]. The shock wave is slightly bent and reaches its maximum strength at a wall-distance of about $\Delta y \approx 0.2$. In the instantaneous contour plots, we can observe

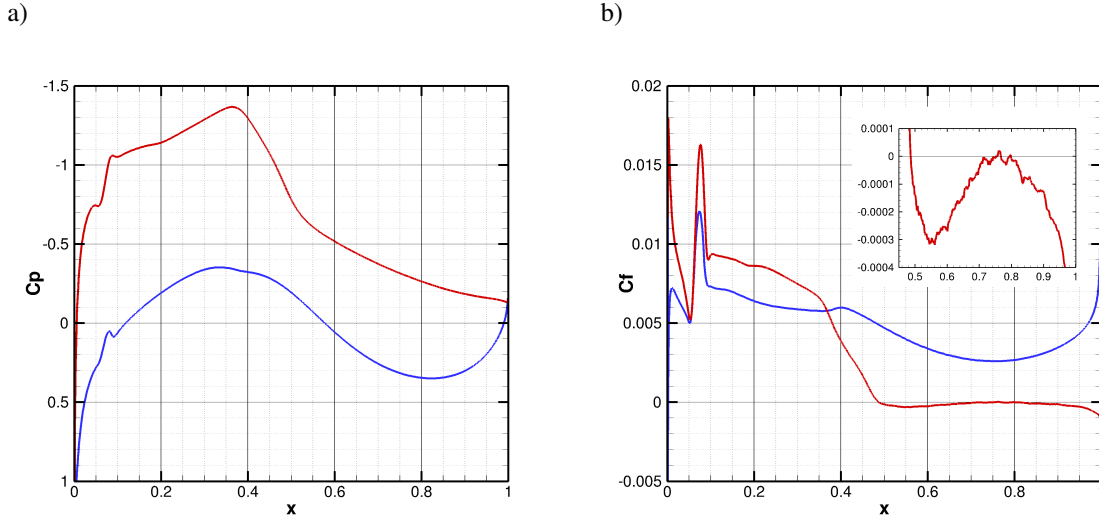


Fig. 10 Time-averaged (a) wall-pressure coefficient C_p and (b) skin-friction coefficient C_f distributions for the OB-3p5-2p8'5p7'3p8'7p8 profile with boundary-layer tripping at $X_{tr} = 0.07$. Blue and red curves correspond to pressure and suction side distributions, respectively.

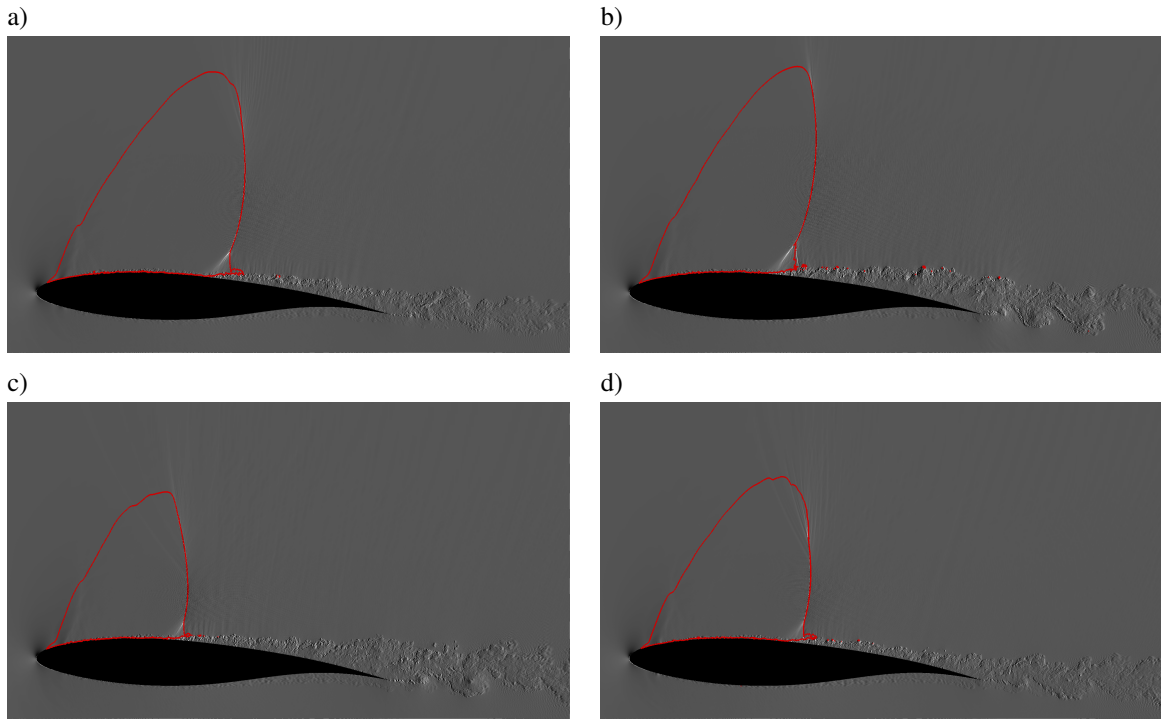


Fig. 11 Numerical quasi-schlieren snapshots showing streamwise density gradients after approximately (a) 53 CTUs (Convective time units), (b) 56 CTUs, (c) 59 CTUs, and (d) 61 CTUs, corresponding to vertical red lines in figure 9. Black and white contours correspond to non-dimensional values of $\partial\rho/\partial x = -20$ and 40 , respectively. Sonic lines are shown in red.

weak non-physical oscillations downstream of the part of the sonic line, which is subjected to the strongest density gradient. However, as they mainly affect the downstream part of the free-stream and not the boundary layers, we did

Snapshot	time instant	C_L	$C_{D,p}$	$C_{D,f}$	C_L/C_D
a)	53.3	high	high	increased	reduced
b)	55.7	increased	high	low	low
c)	58.7	low	reduced	reduced	increased
-	59.7	reduced	low	increased	high
d)	61.15	medium	reduced	high	increased

Table 11 Qualitative overview of aerodynamic properties for snapshots in figure 11.

not apply more frequent filtering when solving the Navier/Stokes equations, which could adversely impact large-scale phenomena [64]. At this time instance, we observe already weak flow separation, which grows continuously until reaching its maximum extent in figure 11(b), where skin-friction drag as well as lift-over-drag ratio hit their minimum. However, as we still observe a large supersonic region, also aerodynamic forces are still increasing. The lift eventually reaches its minimum in snapshot 11(c), where the turbulent boundary layer is already recovering ($C_{D,f}$ is increasing). At the same time the pressure drag keeps decreasing and reaches its minimum slightly delayed at the time instant marked by the grey dash-dotted line in figure 9(b) (no additional snapshot is shown for brevity). In snapshot 11(d), the boundary layer is fully recovered leading to maximum skin-friction drag. When aerodynamic forces are strengthening, boundary layers again start to separate and the cycle starts over again.

Comparing tables 7 and 11, we can see very clear parallels between transonic buffet at free-transitional and tripped conditions across one buffet cycle. Without showing details (histories are provided in the appendix in figure 18), for both baseline cases, C_L histories appear quite sinusoidal. While this remains true for C_D of the tripped case, we observe a saw-tooth pattern (slow increase and rapid decrease) for the free-transitional counterpart, where laminar boundary layers recover relatively fast. Another striking similarity between both cases is the phase shift between C_L and C_D , where lift is leading by about 90° . Given the present observations and detailed discussion of Moise et al. [17], we are confident that we look at the same underlying mechanism for both boundary-layer transition modes, leading to large-scale oscillations of aerodynamic forces associated with transonic buffet.

As for the free-transition cases, we will characterise buffet features for tripped cases by measuring frequencies (St_B) and extreme vales of the lift coefficient ($C_{L,max}$ and $C_{L,min}$, respectively) as well as a maximum amplitude ($\Delta C_{L,max}$). For this baseline case we obtain $\Delta C_{L,max} = 0.24$, $C_{L,max} = 0.85$, $C_{L,min} = 0.61$.

2. Horizontal variation of the upper crest point

Figure 12 shows simulation results for OpenBuffet geometries where the streamwise location of the upper crest point is varied (*i.e.* first digit) between $0.28 \leq X_U \leq 0.32$ ($D_1 = 2.8, 3.0, 3.2$). While C_L histories are shown in figure 7(a), corresponding airfoil geometries are illustrated in (b) in the same manner as in the previous section. Table 12 summarises the parameters used to characterise buffet. Similar to free-transitional cases, we observe decreasing buffet amplitudes when moving the crest point in the downstream direction, while associated frequencies and lift-over-drag ratios increase continuously. For the red curve ($D_1 = 3.2$) in figure 12(a) buffet becomes very weak after an initial transient and we observe a rather irregular behaviour. We do not observe the appearance of the intermediate frequency peak that was seen in free-transitional cases. This is most probably due to significantly smaller separation bubbles for turbulent shock-wave/boundary-layer interactions. It is interesting to note that the mean values (after initial transients) are similar for all curves in figure 12(a).

3. Vertical variation of the upper crest point

Figure 13 shows tripped simulation results for OpenBuffet airfoil geometries where the vertical location of the upper crest point is varied (*i.e.* second digit) between $0.048 \leq Y_U \leq 0.061$ ($D_4 = 4.8, 5.3, 5.7, 6.1$), mainly affecting the airfoil thickness towards the fore part as well as the rounding of the leading edge. Parameters summarised in table 13 confirm these trends. Again similar to free-transitional cases, we observe very clear trends. Reducing the thickness via Y_U , buffet frequencies and associated amplitudes decrease. While buffet appears to be intermittent for case OB-T-D2-4p8, the mean lift settles around maximum C_L -levels of the baseline test case. Also similar to the free-transitional cases, the lift-over-drag ratios increase with decreasing Y_U . For the considered profiles at tripped conditions, we do not observe

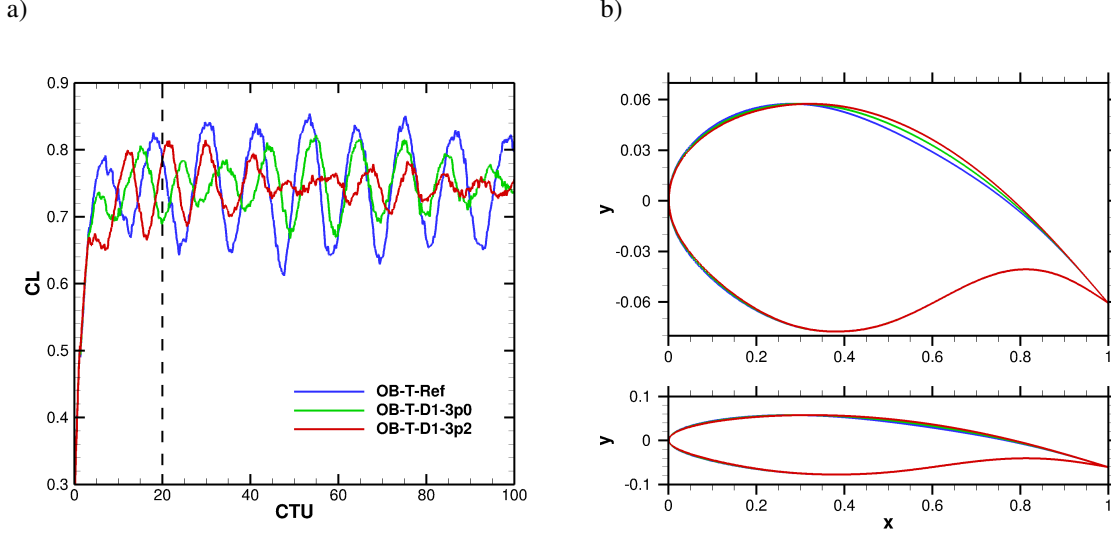


Fig. 12 (a) Lift coefficient (C_L) as a function of convective time units (CTU) for 4-digit OB airfoils at an angle of attack $\alpha = 3.5^\circ$, where the first digit is varied for tripped simulations. Corresponding airfoil contours are shown in (b), respectively, where the aspect ratio of the upper plot axes is distorted. The aspect ratio of the lower plot is $x:y=1:1$.

Case	D_1	St_B	$\Delta C_{L,max}$	$C_{L,max}$	$C_{L,min}$	$C_{D,max}$	$C_{D,min}$	$\overline{L/D}$
OB-T-Ref	2.8	0.088	0.24	0.85	0.61	0.061	0.035	15.1
OB-T-D1-3p0	3.0	0.100	0.15	0.82	0.67	0.055	0.037	16.4
OB-T-D1-3p2	3.2	0.113	0.13	0.81	0.69	0.053	0.036	17.3

Table 12 Summary of buffet characteristics for tripped cases varying the first digit of the reference case OB-T-Ref considering the OB-3p5-2p8’5p7’3p8’7p8 profile.

intermediate frequencies arising when buffet becomes weak.

IV. Buffet sensitivities for flattened versions of the OpenBuffet geometries

In this section, we will consider a slightly modified version of the OpenBuffet parametric airfoil geometries, denoted by ‘OBF’. For the same airfoil designation, this is used to check the sensitivity to the upper surface curvature distribution and simultaneously allows a wider parametric study. To obtain a slightly flatter airfoil shape downstream of the crest point, the second derivatives at the crest points have been set to zero ($Y''_U(x = X_U) = Y''_L(x = X_L) = 0$). This avoids an inflection point of the polynomials connecting crest points and trailing edge for combinations of parameters leading to a relatively small radius near the crest (*e.g.* low X_U values). Figure 14 shows examples with distorted coordinates for clarity to illustrate the problem. Starting from $X_U = 0.35$, the streamwise position of the upper crest point is incrementally reduced for 4-digit profiles. Original and modified OpenBuffet geometries are denoted by solid and dashed curves, respectively. While the differences are relatively small for $X_U \geq 0.3$, we see the appearance of an inflection point in the original OB-4-2p5666 profile (orange curves), which is absent in the OBF-4-2p5666 profile. Even though the modified profile also shows an deflection point for the very extreme case of $X_U = 0.2$ (red curves), it is significantly less pronounced compared to the original version.

This modification allows us to cover an extended parameter range and is also used to assess buffet sensitivities to the shape of the polynomial connecting crest points and trailing edge. We will limit this study to free-transitional test cases, as we expect similar trends for the (computationally more expensive) tripped cases. For free-transitional test cases, we can also study sensitivities of intermediate-frequency phenomena, which have not been observed for the tripped cases

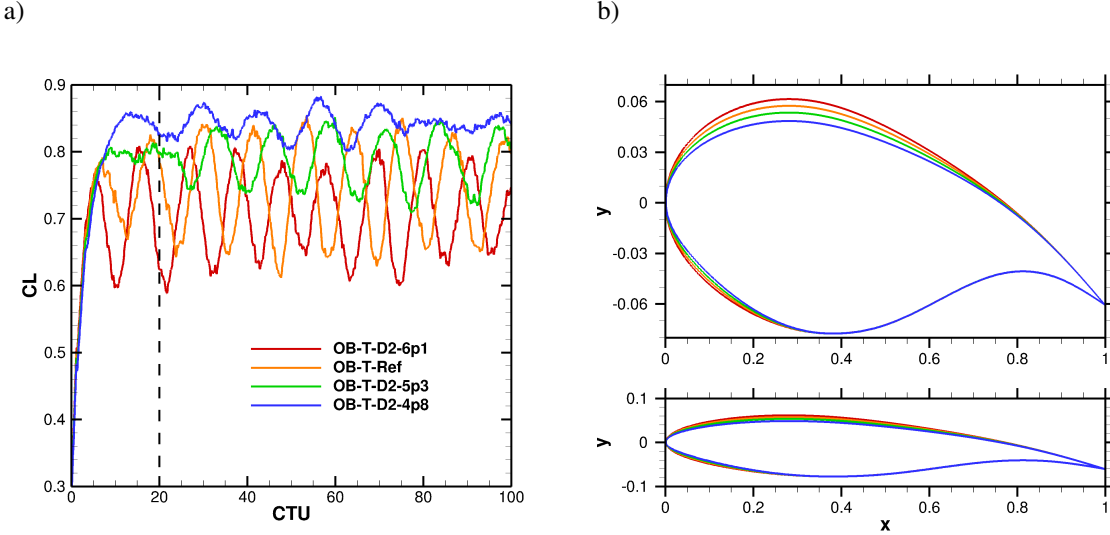


Fig. 13 (a) Lift coefficient (C_L) as a function of convective time units (CTU) for 4-digit OB airfoils at an angle of attack $\alpha = 4^\circ$, where the second digit is varied for tripped simulations. Corresponding airfoil contours are shown in (b), respectively, where the aspect ratio of the upper plot axes is distorted. The aspect ratio of the lower plot is x:y=1:1.

Case	D_2	St_B	$\Delta C_{L,max}$	$C_{L,max}$	$C_{L,min}$	$C_{D,max}$	$C_{D,min}$	$\overline{L/D}$
OB-T-D2-6p1	6.1	0.100	0.22	0.81	0.59	0.065	0.038	13.6
OB-T-Ref	5.7	0.088	0.24	0.85	0.61	0.061	0.035	15.1
OB-T-D2-5p3	5.3	0.075	0.14	0.85	0.71	0.055	0.037	17.2
OB-T-D2-4p8	4.8	0.075	0.08	0.88	0.8	0.047	0.038	19.9

Table 13 Summary of buffet characteristics for tripped cases, varying the second digit of the reference case OB-T-Ref considering the OB-3p5-2p8'5p7'3p8'7p8 profile.

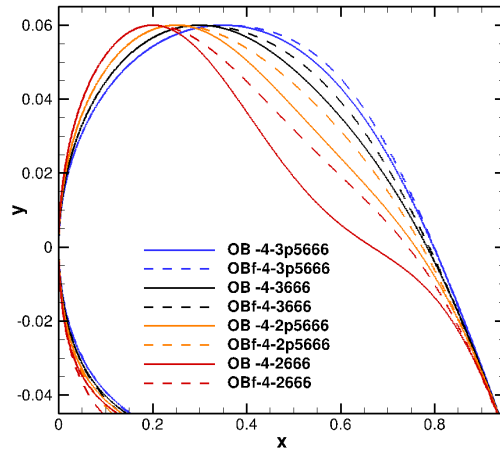


Fig. 14 Comparison of original OpenBuffet geometries (solid curves) and modified versions (dashed curves).

Case	D_1	St_B	St_I	$\Delta C_{L,max}$	$C_{L,max}$	$C_{L,min}$	$C_{D,max}$	$C_{D,min}$	\bar{L}/\bar{D}
4-OBf-3666	3	0.115	0.520	0.51	1.15	0.64	0.100	0.044	12.6
4-OB -3666	3	0.115	-	0.46	1.09	0.63	0.102	0.039	12.4
4-OBf-3p5666	3.5	0.165	0.657	0.28	1.04	0.76	0.085	0.040	15.0
4-OB -3p5666	3.5	0.153	0.615	0.34	1.10	0.76	0.102	0.036	14.3
4-OBf-4666	4	-	0.367	0.32	1.02	0.7	0.116	0.051	10.9
4-OB -4666	4	-	0.338	0.25	0.94	0.69	0.104	0.048	11.1

Table 14 Summary of buffet characteristics comparing original and modified OpenBuffet geometries, varying the first digit.

within the considered parameter space. In this section, test cases labels are composed of the type of geometry (“OBf” or “OB” for flattened or original OpenBuffet profiles), the design angle α_D , and the four digits $D1 - D4$, where the decimal point is replaced by ‘p’.

A. Comparison between flattened and original OpenBuffet profiles

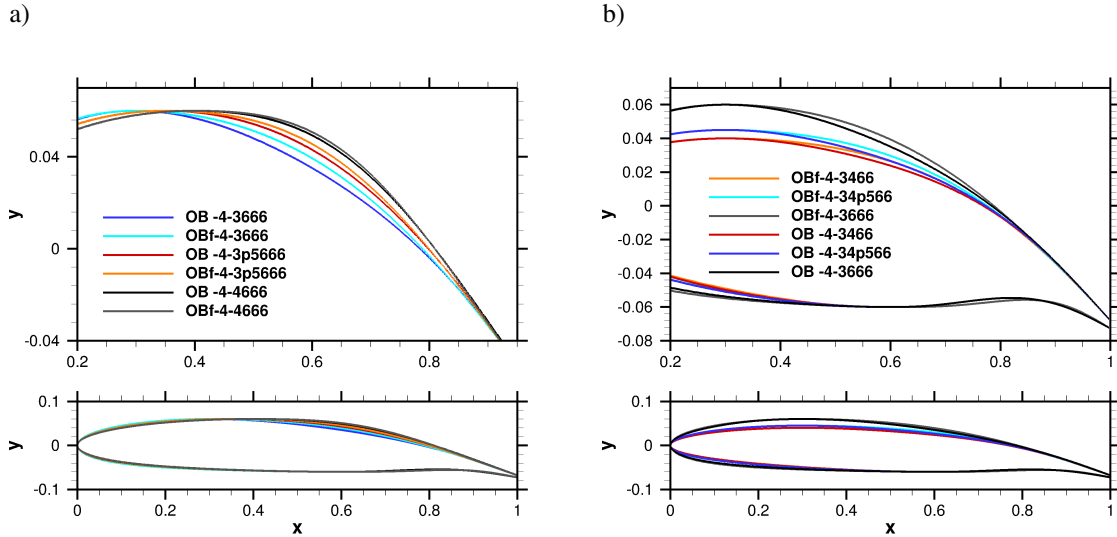


Fig. 15 Selected flattened and original OpenBuffet airfoil profiles for variations of (a) first ($D1$) and (b) second digits ($D2$). While the aspect ratio of the upper plot axes is distorted, the aspect ratio of the lower plot is $x:y=1:1$.

To compare flattened and original OpenBuffet geometries, figure 15 shows a selection of profiles, where (a) the axial and (b) the vertical location of the upper crest point is altered. We observe more pronounced differences for profiles with decreased X_U and/or increased Y_U . For brevity, we will show only tabulated results and provide corresponding lift histories in the appendix §V.C. Table 14 summarises the usual quantities for flattened OBf-profiles and original OB-profiles considering variations of the axial location of the upper crest point ($D1$). While we observe good overall agreement of C_L and aerodynamic performance, we observe moderate variations of C_D . Buffet frequencies seem to be hardly affected by the geometric differences. While spectra for the original OpenBuffet geometry do not exhibit a clear peak for $X_U = 0.3$, we observe one at intermediate frequencies of $St_I = 0.52$ for the modified profile. Based on [16], intermediate frequencies associated with separation-bubble phenomena scale with the length of the separation bubble and maximum reverse velocities, which are highly sensitive to flow conditions.

Table 15 summarises the usual quantities for flattened OBf-profiles and original OB-profiles considering variations of the vertical location of the upper crest point ($D2$). Again, we observe very good agreement in terms of mean properties.

Case	D_2	St_B	St_I	$\Delta C_{L,max}$	$C_{L,max}$	$C_{L,min}$	$C_{D,max}$	$C_{D,min}$	\bar{L}/\bar{D}
4-OBf-3466	4	0.057	0.50	0.09	1.23	1.14	0.057	0.041	24.8
4-OB -3466	4	0.050	0.55	0.06	1.19	1.12	0.051	0.040	25.0
4-OBf-34p566	4.5	0.077	0.54	0.15	1.18	1.03	0.062	0.035	22.9
4-OB -34p566	4.5	0.077	0.57	0.20	1.17	0.96	0.059	0.033	22.3
4-OBf-3666	6	0.115	0.52	0.51	1.15	0.64	0.100	0.044	12.6
4-OB -3666	6	0.115	-	0.46	1.09	0.63	0.102	0.039	12.4

Table 15 Summary of buffet characteristics comparing original and modified OpenBuffet geometries, varying the second digit.

Extreme values for C_L and C_D do not show significant sensitivities to the geometric modifications. While buffet frequencies show excellent agreement for cases with $Y_U = 0.06$ and 0.045 , we observe some variations for $Y_U = 0.04$. Also for these cases, intermediate frequencies show slightly increased sensitivities to the geometric variations.

Overall, we can confirm the same trends for modified as well as original OpenBuffet geometries, when varying the upper crest position. We do observe difference of extreme values for C_L and C_D (which may be also due to limited run times), but mean flow quantities (*e.g.* \bar{L}/\bar{D}) show very good agreement. Also, while buffet frequencies show minor sensitivities, reduced curvature (flatter profiles) seems to promote separation-bubble instabilities at intermediate frequencies as well as shifting St_I for most cases to lower frequencies. According to Zauner et al. [16], this may be due to reduced separation bubble length or decreased reverse velocities.

B. Analysis of extended parameter space using flattened OpenBuffet profiles

As mentioned at the beginning of this section, the flattened OpenBuffet profiles allow us to study an extended parameter space without additional inflection points appearing within the rear part of the suction side. Table 16 shows a summary of our usual quantities to characterise aerodynamic properties and buffet phenomena for all selected cases. For brevity, we will focus here on quantitative results of this table and provide full histories for all cases in appendix §V.E.

The first (upper) section of table 16 contains simulation results for variations of the axial position on the upper crest point. Given the additional simulation with $X_U = 0.25$, it indeed seems as the axial position may impact buffet on-set and off-set characteristics. Buffet amplitudes increase from $X_U = 0.25$ to $X_U = 0.30$ before incrementally decreasing again for $X_U > 0.30$. While the shock position moves downstream when increasing X_U , flow separation on the rear part of the airfoil is promoted by the steep slope of the upper surface contour. Eventually we observe off-set conditions at $X_U = 0.40$. Tendencies of C_L , C_D , and lift-over-drag ratio align with this explanation as well. Clear trends are also observed in the second section of table 16, where buffet frequencies as well as amplitudes continuously increase with increasing Y_U . Separation-bubble instabilities at intermediate frequencies do not seem to be significantly affected, but they become less pronounced for $Y_U = 0.05$, where drag is low.

While the upper crest points have already been analysed for original OpenBuffet geometries as well, the lower (pressure side) crest-point locations have only been studied for the flattened OpenBuffet profiles of this section. Geometries are shown in figure 16 and corresponding simulation results are summarised in the bottom two sections of table 16. Although the axial location of the lower crest point (X_L) shows hardly any influence on the aerodynamic properties or buffet characteristics at present conditions, we do observe influence of the vertical location Y_L . We should emphasise that the lower crest point becomes concave for $D_4 = 3$. While the inflection point of the lower-side geometry is usually located between the lower crest and the trailing edge, it shifts in the upstream direction when increasing Y_L . For the red profile in figure 16(b), the axial location of the inflection point is eventually located upstream of X_L . Nonetheless, this effect shows no significant effect on the buffet characteristics, even though aerodynamic forces increase with increasing Y_L . Intermediate frequencies, however, tend to decrease with increasing Y_L . When moving from $D_4 = 6$ to $D_4 = 9$, however, we observe a decrease of the buffet frequency, but no significant changes in the lift-over-drag ratio.

Figure 17 shows buffet frequency (top plot), buffet amplitude (center plot), and maximum lift (bottom plot) as a function of the crest-to-crest thickness ($Y_U - Y_L$). Simulation results for variations of the vertical crest position of the upper and lower sides are denoted by red and blue symbols, respectively. Adjusting the suction side, the buffet frequency increases almost linearly with the crest-to-crest thickness. Variations of the crest-to-crest thickness via the

Case	D_x	St_B	St_I	$\Delta C_{L,max}$	$C_{L,max}$	$C_{L,min}$	$C_{D,max}$	$C_{D,min}$	\bar{L}/\bar{D}
4-OBf-2p5666	$D_1 = 2.5$	0.128	0.43	0.41	0.99	0.59	0.122	0.032	11.6
4-OBf-3666	$D_1 = 3$	0.115	0.52	0.51	1.15	0.64	0.100	0.044	12.6
4-OBf-3p5666	$D_1 = 3.5$	0.165	0.66	0.28	1.04	0.76	0.085	0.040	15.0
4-OBf-4666	$D_1 = 4$	-	0.37	0.32	1.02	0.70	0.116	0.051	10.8
4-OBf-3466	$D_2 = 4$	0.057	0.50	0.09	1.23	1.14	0.057	0.041	24.8
4-OBf-34p566	$D_2 = 4.5$	0.077	0.53	0.15	1.18	1.03	0.062	0.035	22.9
4-OBf-3566	$D_2 = 5$	0.096	0.52-0.61	0.40	1.19	0.79	0.079	0.031	18.3
4-OBf-3666	$D_2 = 6$	0.115	0.52	0.51	1.15	0.64	0.100	0.044	12.6
4-OBf-3766	$D_2 = 7$	0.134	0.63	0.48	1.13	0.65	0.130	0.051	10.2
4-OBf-3646	$D_3 = 4$	0.115	0.40	0.49	1.20	0.71	0.111	0.044	12.7
4-OBf-3656	$D_3 = 5$	0.115	0.52	0.48	1.17	0.68	0.117	0.041	12.5
4-OBf-3666	$D_3 = 6$	0.115	0.52	0.51	1.15	0.64	0.100	0.044	12.6
4-OBf-3663	$D_4 = 3$	0.115	0.46	0.43	1.30	0.87	0.120	0.050	13.2
4-OBf-3666	$D_4 = 6$	0.115	0.52	0.51	1.15	0.64	0.100	0.044	12.6
4-OBf-3669	$D_4 = 9$	0.096	0.54	0.45	0.89	0.44	0.074	0.034	12.6

Table 16 Summary of buffet characteristics for flattened OpenBuffet geometries considering variations of $D_1 - D_4$. Each section of the table shows variations of a single digit.

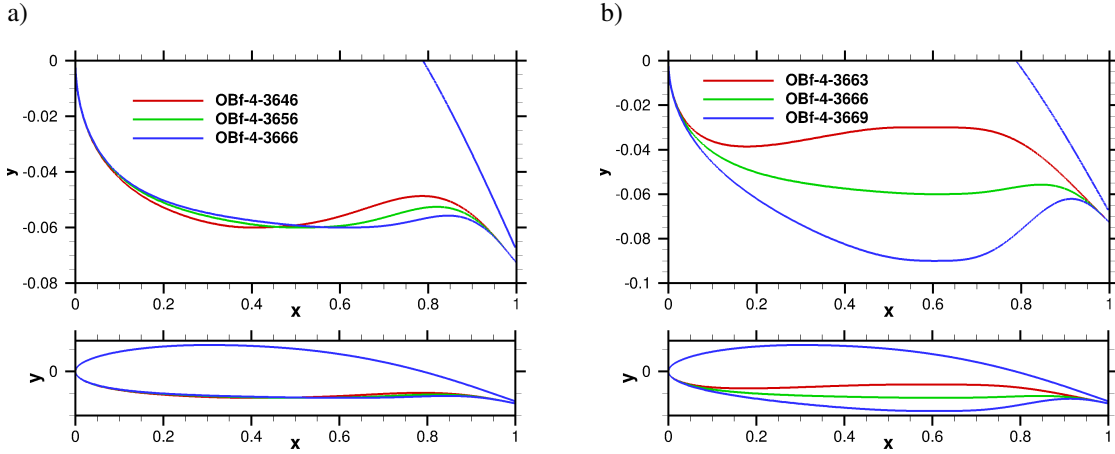


Fig. 16 Flattened OpenBuffet airfoil profiles for variations of (a) third (D_3) and (b) fourth digits (D_4). While the aspect ratio of the upper plot axes is distorted, the aspect ratio of the lower plot is $x:y=1:1$

lower crest position show only little effect. Looking at the $\Delta C_{L,max}$ associated with the buffet amplitude, we observe an initial increase, peaking at a crest-to-crest thickness of 0.12. When buffet is established, amplitudes show only minor sensitivity to changes of the crest-to-crest thickness. The maximum lift, however, shows a common trend across all simulations modifying Y_U or Y_L . Despite some variations, it steadily decreases with increasing crest-to-crest thickness. Black lines indicate a corridor corresponding to a $\Delta C_L = 0.14$ (corresponding to approximately 10% of $C_{L,max}$) for visual aid with respect to the spread of results. Due to the complex nature of present simulations and limited run-time such variations are not surprising. For longer run times and statistical convergence, the corridor containing simulation results may become narrower.

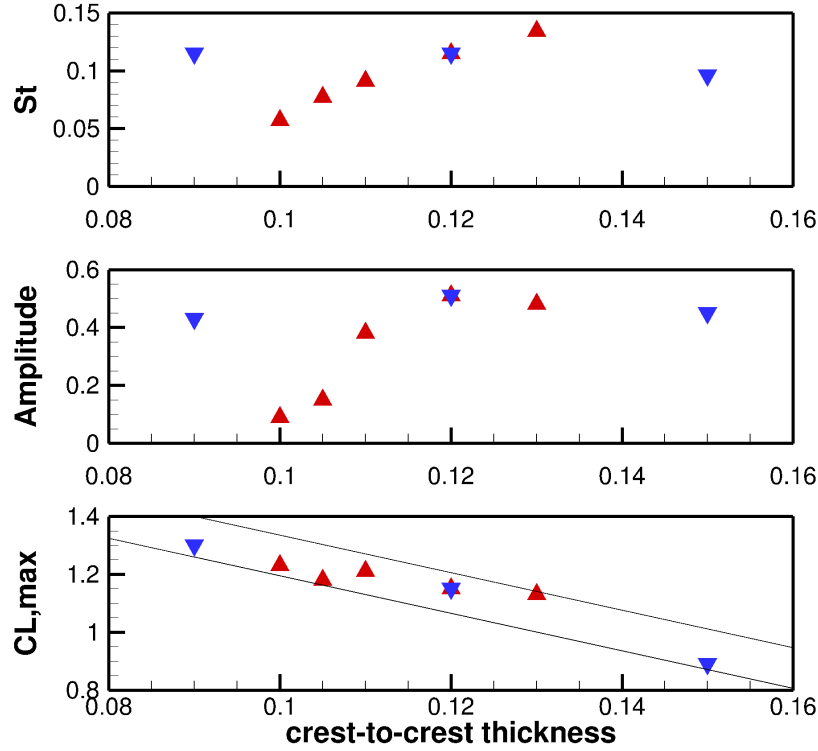


Fig. 17 Buffet frequency (top), amplitude (center), and maximum lift (bottom) as a function of the crest-to-crest thickness ($Y_U - Y_L$). Red and blue symbols denote variations of Y_U and Y_L , respectively.

V. Conclusions

An airfoil construction method has been devised to explore the geometric sensitivities of large-scale oscillations at typical buffet conditions in an intuitive way. Using Large-Eddy Simulations, an extensive parametric study has been carried out for four-digit OpenBuffet profiles considering free-transitional as well as tripped boundary layers at moderate Reynolds numbers of $Re = 500,000$.

General trends for variations of the suction-side geometry agree very well for both free-transitional and tripped boundary-layer conditions. We observe significant influence of the upper-side crest location to buffet on- and off-set conditions. Shifting the upper crest towards the trailing edge promotes buffet off-set, while promoting separation effects and intermediate-frequency phenomena for free-transitional cases. Within the considered parameter space, no intermediate-frequency phenomena associated with separation-bubble instabilities have been observed for tripped cases. Reducing the airfoil thickness via the vertical location of the upper crest (Y_U) tends to stabilise the flow and increase the aerodynamic efficiency. Also the Strouhal number of the buffet frequency increases with Y_U . The maximum lift coefficient, however, does not change significantly. A similar trend was observed in [16] when increasing the Mach number for ONERA's OALT25 profile at a fixed angle of attack. Variations of the axial location of the pressure-side crest show minor impact and can be neglected for future studies. The vertical displacement of the crest, however, can affect levels of maximum as well as buffet frequencies.

Scaling of intermediate frequencies based on mean-flow properties of the separation bubble was applied to the OB-F-D2-4p5 test case (OB-4-34p566 profile) and agrees well with reference data of different airfoil geometries in [16].

Modified versions of the OpenBuffet geometries have been studied as well, where the upper-side geometry downstream of the crest is slightly flattened to increase the parameter space. Flatter profiles show small effects on mean properties, but promote intermediate-frequency phenomena.

For present airfoil geometries, the maximum lift levels scale well with the crest-to-crest thickness. For cases with established buffet, the crest-to-crest thickness has a minor effect on buffet amplitudes. Buffet frequencies scale almost linearly with variations of the vertical position of the upper crest point. Therefore, the airfoil thickness is not sufficient to explain differences of frequencies between different airfoils. Instead, the upper crest location of the rotated airfoil

shows significant influence on buffet characteristics. For a given geometry, buffet characteristics do not only depend on the shape at zero inclination, but also the angle of attack, which has significant influence on the crest locations.

The present study provides data for a wide parameter range, which can be used by the research community for comparison with lower-fidelity methods like RANS or URANS. Present OpenBuffet geometries are publicly available via <https://doi.org/10.5281/zenodo.12204411>.

Appendix

A. Comparison of tripped and free-transitional OpenBuffet reference cases

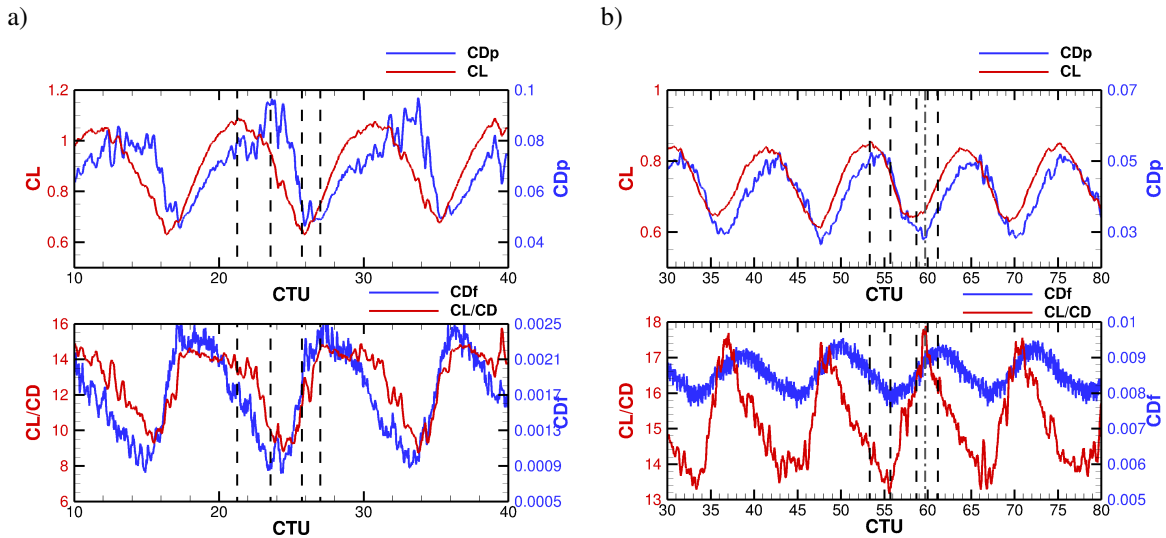


Fig. 18 Histories of aerodynamic coefficients for OpenBuffet airfoils considering (a) free-transitional (OB-4-3666) and (b) turbulent boundary layers (OB-3p5-2p8'4p8'3p8'7p8).

Comparing tables 7 and 11 of the main text, we can see very clear parallels between transonic buffet at free-transitional and tripped conditions. Figure 18 provides additional histories for (a) free-transitional and (b) tripped reference cases. Top plots show lift coefficient C_L (red curves and left-hand-side scale) and pressure-drag coefficient $C_{D,p}$ (blue curves and right-hand-side scale) as a function of convective time units. Bottom plots show lift-over-drag ratio C_L/C_D (red curves and left-hand-side scale) and skin-friction-drag coefficient $C_{D,f}$ (blue curves and right-hand-side scale) as a function of convective time units. For both baseline cases, C_L histories are approximately sinusoidal. While this remains true for $C_{D,p}$ of the tripped case, we observe a saw-tooth pattern (slow increase and rapid decrease) for the free-transitional counterpart. For $C_{D,f}$ of free-transitional cases, the saw-tooth pattern is reversed, as we observe rapid increase and slower decay. For the turbulent case, the $C_{D,f}$ history appears slightly skewed. As boundary layers recover much faster for the free-transitional case, we observe some sort of plateau for $C_{D,f}$ as well as lift-over-drag histories. The latter appears very spiky with flat troughs for the tripped case. Buffet amplitudes are notably higher for the free-transitional case compared to the tripped case. Despite some variations in signal shapes, a striking similarity between both cases is the phase shift between C_L and C_D , where lift leads drag by about 90° .

B. Additional data for free-transitional test cases

Figure 19 shows time-averaged suction-side (a) wall-pressure and (b) skin-friction coefficients for free-transitional cases varying the upper crest location. Differences between the blue (OB-4-3666 airfoil) and the black (OB-4-3p5666 airfoil) curves are mainly due to a down-stream shift of the mean shock-wave position. Further downstream displacement of the upper crest leads to significantly reduced suction for the red curve (OB-4-4666 airfoil) in figure 19(a), while the trailing edge pressure diverges significantly due to increased flow separation. We can observe in figure 19(b) that only the blue curve shows clear re-attachment of the mean flow. For increasing X_U , C_f levels decrease due to the dominance of separation phenomena. These tendencies are very reminiscent of buffet off-set or incipient stall.

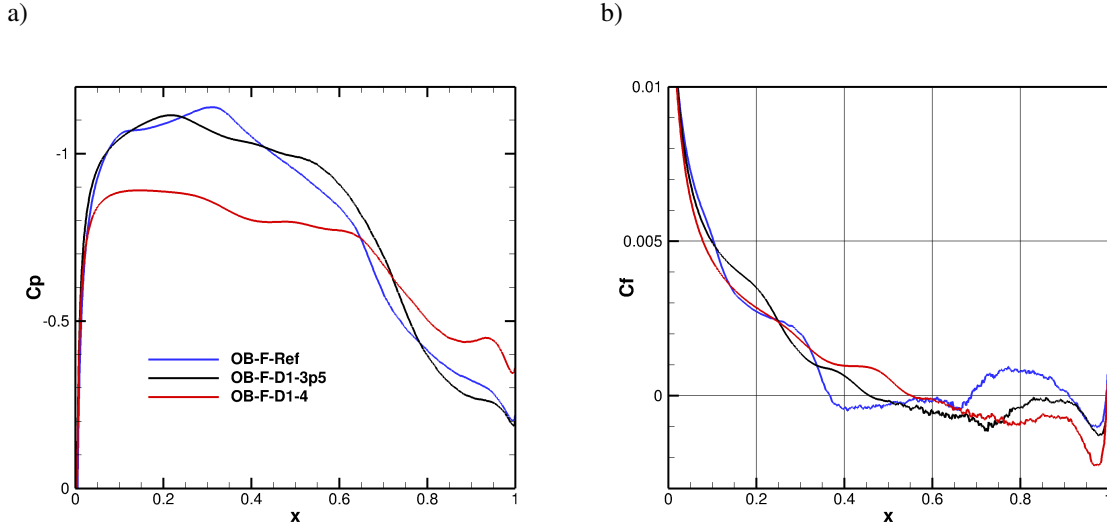


Fig. 19 Distributions of suction-side (a) wall-pressure and (b) skin-friction coefficients for free-transitional cases varying the upper crest location.

C. Comparison between flattened and original OpenBuffet profiles

Lift histories of free-transitional LES are shown for both, flattened and original OpenBuffet profiles. Figure 21

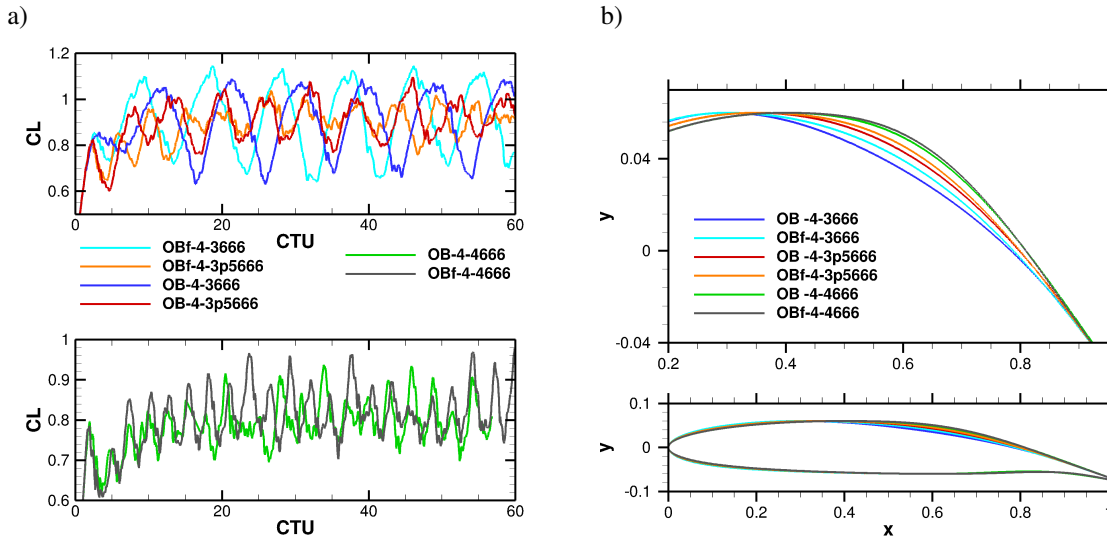


Fig. 20 (a) Lift coefficient (C_L) as a function of convective time units (CTU) for 4-digit airfoils at an angle of attack $\alpha = 4^\circ$, where the first digit is varied for modified (OBf-4-X666) and original OB-4-X666 profiles. Corresponding airfoil contours are shown in (b), respectively, where the aspect ratio of the upper plot axes is distorted. The aspect ratio of the lower plot is $x:y=1:1$.

shows (a) histories and (b) corresponding geometries for variations of the vertical position of the upper crest point. Figure 20 shows (a) histories and (b) corresponding geometries for variations of the axial position of the upper crest point. All in all, we can confirm good qualitative agreement for both airfoil families.

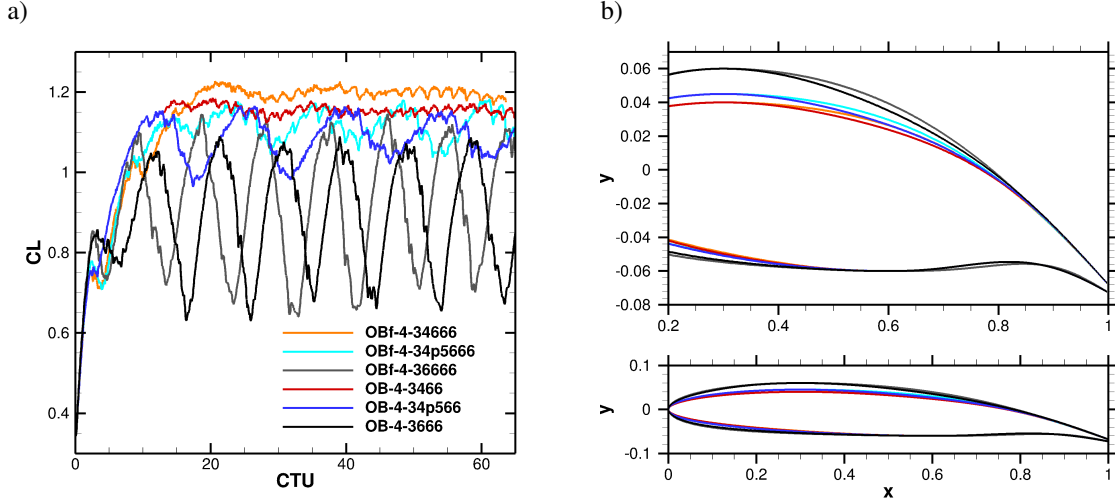


Fig. 21 (a) Lift coefficient (C_L) as a function of convective time units (CTU) for 4-digit airfoils at an angle of attack $\alpha = 4^\circ$, where the second digit for modified (OBf-4-X666) and original OB-4-X666 profiles. Corresponding airfoil contours are shown in (b), respectively, where the aspect ratio of the upper plot axes is distorted. The aspect ratio of the lower plot is $x:y=1:1$.

D. Data used for scaling intermediate frequencies of case OB-F-D2-4p5

For a selected test case, we attempt a scaling approach of the intermediate-frequency phenomenon proposed by [16]. We consider test case OB-F-34p566 (OB-4-34p566 profile) of section III.A. In a LES study of ONERA's OALT25 airfoil at similar flow conditions, [16] scaled the Strouhal number St_I associated with an unsteady recirculation bubble with mean-flow properties of the separation bubble. To obtain the scaled Strouhal number St_R , the chord-based Strouhal number St_I needs to be multiplied by the normalised mean separation length L_{sep}/c and the maximum reverse velocity U_R/U_∞ observed in the mean flow within the separation bubble. The latter is approximated by the minimum streamwise mean-velocity component, which is shown in figure 22(a). Blue and red contours show respectively negative and positive values of the streamwise mean-velocity component U_x , while the green iso-curve delineates a region of $U_x/U_\infty < -0.1$, which contains $U_R/U_\infty = |U_x/U_\infty| = 0.102$. Figure 22(b) shows the distribution of the time-averaged skin-friction coefficient C_f (using a reduced sampling rate of 0.035 CTUs), where we can extract the mean length of the separation bubble, bounded by the vertical dashed blue lines delivering $L_{sep}/c = 0.356$. The Strouhal number $St_I = 0.573$ associated with the intermediate-frequency phenomenon is provided in table 9 for the test case OB-F-D2-4p5. Applying now the scaling according to [16], we obtain $St_R = St_I L_{sep}/c U_R/U_\infty = 0.573 \cdot 0.356 \cdot 0.102 = 0.021$. This scaled frequency agrees very well with those of various airfoil profiles in [16]. For ONERA's OALT25 profile they reported at the same Mach- and Reynolds number $St_R = 0.022$ and for Dassault Aviations's V2C profile $St_R = 0.023$. The Strouhal numbers without scaling are very different, reading $St_I = 0.42$ and 0.6 , respectively.

E. Histories of flattened OpenBuffet profiles

Additional histories are provided for the modified OpenBuffet geometries with flattened crest. Figures 24 and 23 show variations of the upper crest point, while figures 25 and 26 show variations of the lower crest point. Plots (a) and (b) show C_L histories and corresponding geometries, respectively.

Acknowledgments

The authors want to acknowledge the Iridis5 (University of Southampton) and JSS3 (JAXA) supercomputing facilities and associated staff for providing computational resources and technical support. Neil D. Sandham acknowledges the support of EPSRC project EP/W026686/1. David J. Lusher has been funded by the Japan Society for the Promotion of Science (JSPS), on a postdoctoral fellowship awarded to the JAXA Chofu Aerospace Center. Additional funding was provided by a JSPS KAKENHI grant award (22F22059). The authors also want to thank ONERA and Dassault Aviation for providing OAT15A, OALT25, and V2C airfoil geometries. This manuscript has been submitted for presentation at

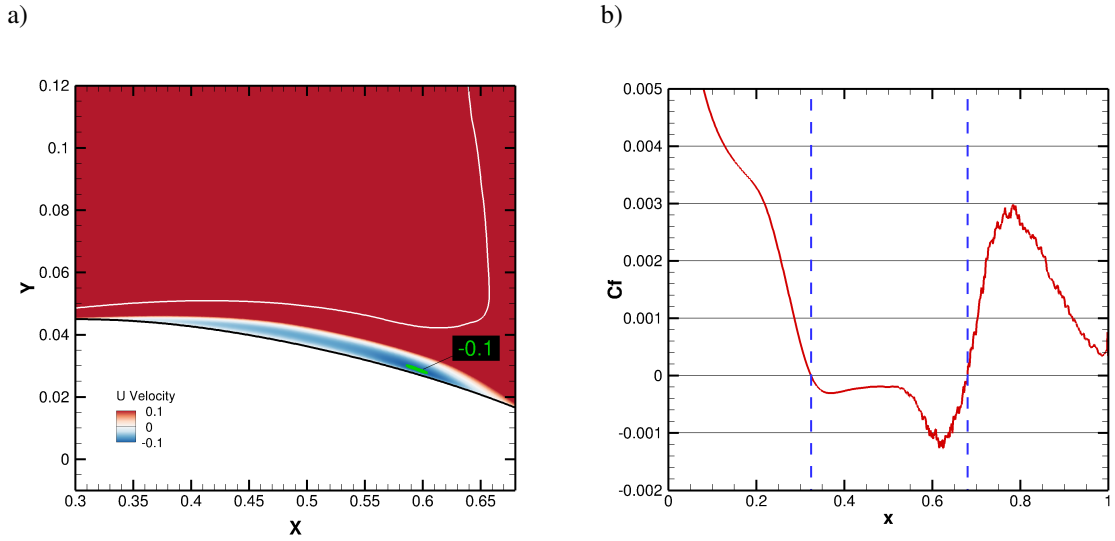


Fig. 22 (a) Streamwise mean-velocity component and (b) suction-side skin-friction distribution for free-transitional case OB-F-D2-4p5 using the OB-4-34p566 profile.

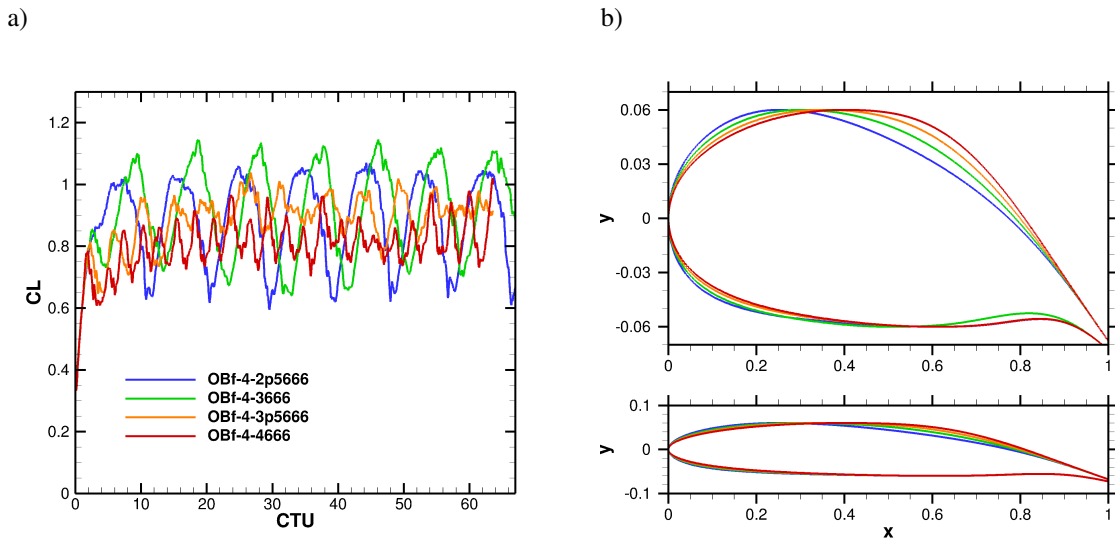


Fig. 23 (a) Lift coefficient (C_L) as a function of convective time units (CTU) for 4-digit airfoils at an angle of attack $\alpha = 4^\circ$, where the first digit is varied (OBf-4-X666). Corresponding airfoil contours are shown in (b), respectively, where the aspect ratio of the upper plot axes is distorted. The aspect ratio of the lower plot is $x:y=1:1$.

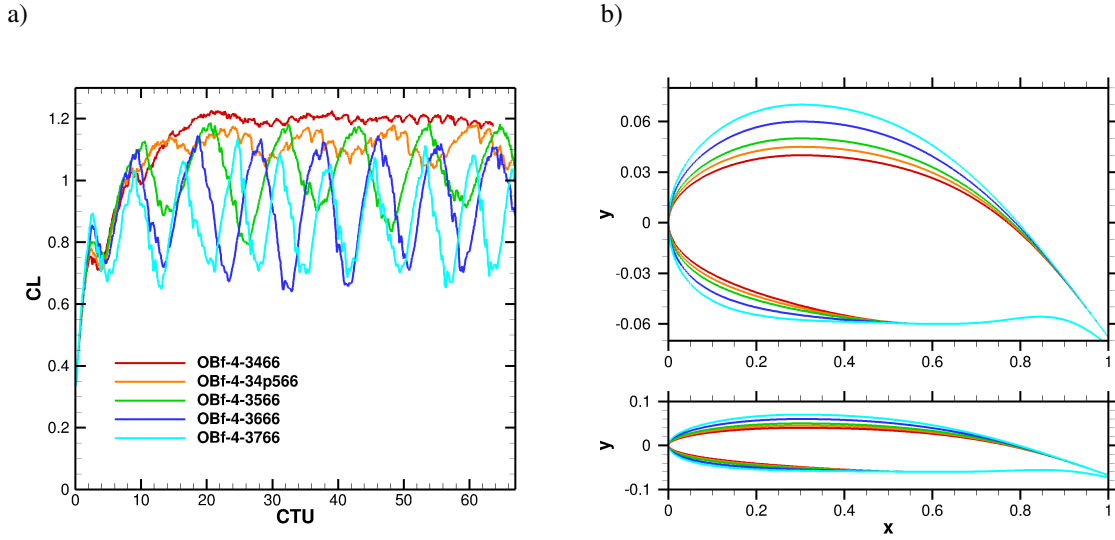


Fig. 24 (a) Lift coefficient (C_L) as a function of convective time units (CTU) for 4-digit airfoils at an angle of attack $\alpha = 4^\circ$, where the second digit is varied (OBf-4-3X66). Corresponding airfoil contours are shown in (b), respectively, where the aspect ratio of the upper plot axes is distorted. The aspect ratio of the lower plot is $x:y=1:1$.

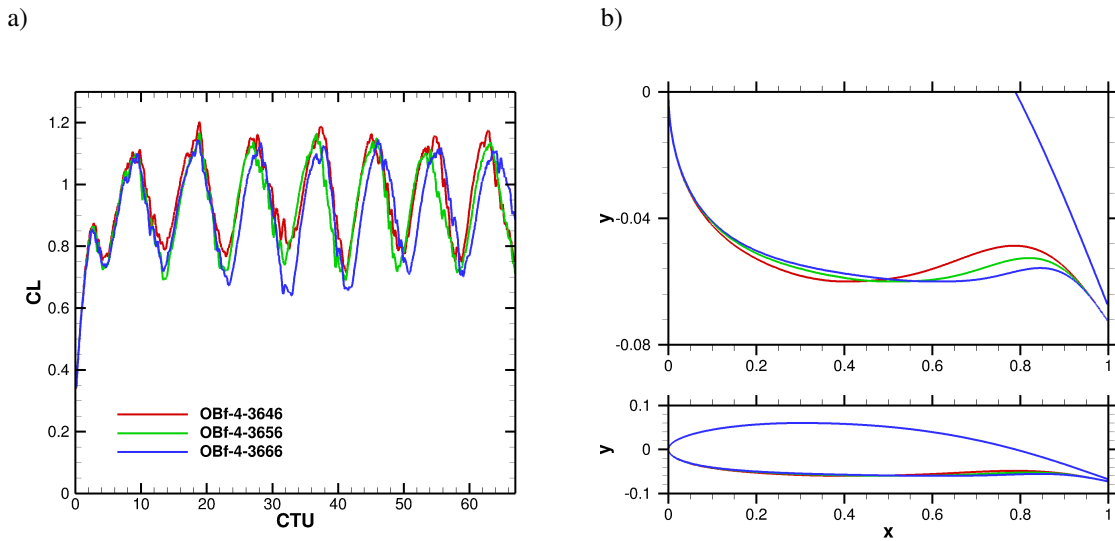
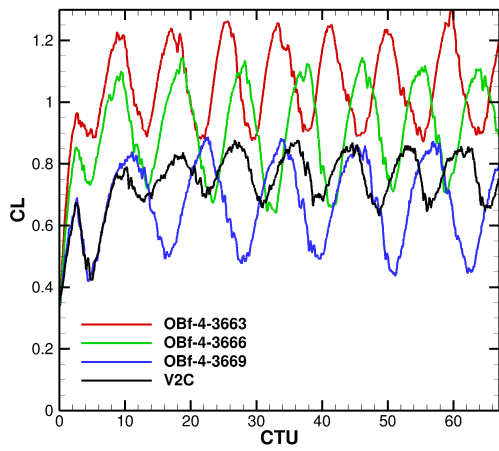


Fig. 25 (a) Lift coefficient (C_L) as a function of convective time units (CTU) for 4-digit airfoils at an angle of attack $\alpha = 4^\circ$, where the third digit is varied (OBf-4-36X6). Corresponding airfoil contours are shown in (b), respectively, where the aspect ratio of the upper plot axes is distorted. The aspect ratio of the lower plot is $x:y=1:1$. Please note that the upper side is constant for all profiles shown.

a)



b)

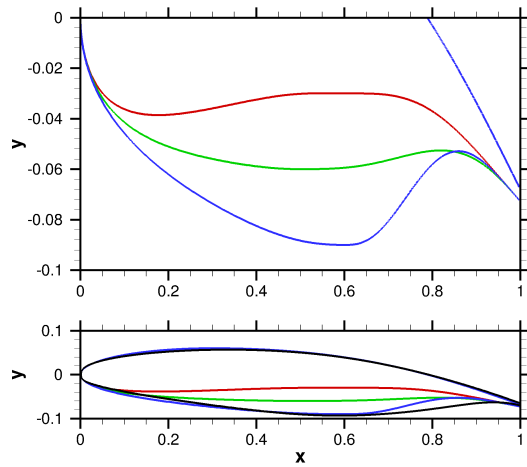


Fig. 26 (a) Lift coefficient (C_L) as a function of convective time units (CTU) for 4-digit airfoils at an angle of attack $\alpha = 4^\circ$, where the fourth digit is varied (OBF-4-366X). Black curves correspond to data for the V2C profile taken from [14]. Corresponding airfoil contours are shown in (b), respectively, where the aspect ratio of the upper plot axes is distorted. The aspect ratio of the lower plot is $x:y=1:1$ and contains also Dassault Aviation's V2C profile, which it is not included in the distorted plot. Please note that the upper side is constant for all profiles shown.

References

- [1] Plante, F., Dandois, J., Beneddine, S., Laurendeau, E., and Sipp, D., “Link between subsonic stall and transonic buffet on swept and unswept wings: from global stability analysis to nonlinear dynamics,” *Journal of Fluid Mechanics*, Vol. 908, 2021.
- [2] Moise, P., Zauner, M., and Sandham, N. D., “Connecting transonic buffet with incompressible low-frequency oscillations on aerofoils,” *Journal of Fluid Mechanics*, Vol. 981, 2024, p. A23. <https://doi.org/10.1017/jfm.2023.1065>.
- [3] Crouch, J. D., Garbaruk, A., and Strelets, M., “Global Instability Analysis of Unswept- and Swept-Wing Transonic Buffet Onset,” *2018 Fluid Dynamics Conference*, 2018. <https://doi.org/10.2514/6.2018-3229>, URL <https://arc.aiaa.org/doi/10.2514/6.2018-3229>.
- [4] Timme, S., and Thormann, R., “Towards Three-Dimensional Global Stability Analysis of Transonic Shock Buffet,” *AIAA Atmospheric Flight Mechanics Conference*, Vol. 3848, American Institute of Aeronautics and Astronautics, Reston, Virginia, 2016, pp. 1–13. <https://doi.org/10.2514/6.2016-3848>, URL <http://arc.aiaa.org/doi/10.2514/6.2016-3848>.
- [5] Sansica, A., and Hashimoto, A., “Global Stability Analysis of Full-Aircraft Transonic Buffet at Flight Reynolds Numbers,” *AIAA Journal*, Vol. 61, No. 10, 2023, pp. 4437–4455. <https://doi.org/10.2514/1.J062808>, URL <https://doi.org/10.2514/1.J062808>.
- [6] Paladini, E., Beneddine, S., Dandois, J., Sipp, D., and Robinet, J.-C., “Transonic buffet instability: From two-dimensional airfoils to three-dimensional swept wings,” *Physical Review Fluids*, Vol. 4, No. 10, 2019, p. 103906. <https://doi.org/10.1103/PhysRevFluids.4.103906>, URL <https://doi.org/10.1103/PhysRevFluids.4.103906><https://link.aps.org/doi/10.1103/PhysRevFluids.4.103906>.
- [7] Ohmichi, Y., Ishida, T., and Hashimoto, A., “Modal Decomposition Analysis of Three-Dimensional Transonic Buffet Phenomenon on a Swept Wing,” *AIAA Journal*, Vol. 56, No. 10, 2018, pp. 3938–3950. <https://doi.org/10.2514/1.J056855>, URL <https://arc.aiaa.org/doi/10.2514/1.J056855>.
- [8] D’Aguanno, A., Schrijer, F. F. J., and van Oudheusden, B. W., “Spanwise organization of upstream traveling waves in transonic buffet,” *Physics of Fluids*, Vol. 33, No. 10, 2021, p. 106105. <https://doi.org/10.1063/5.0062729>, URL <https://doi.org/10.1063/5.0062729>.
- [9] Iovnovich, M., and Raveh, D. E., “Reynolds-Averaged Navier-Stokes Study of the Shock-Buffet Instability Mechanism,” *AIAA Journal*, Vol. 50, No. 4, 2012, pp. 880–890. <https://doi.org/10.2514/1.J051329>, URL <http://arc.aiaa.org/doi/10.2514/1.J051329>.
- [10] Lusher, D. J., Sansica, A., Zauner, M., and Hashimoto, A., “High-fidelity study of three-dimensional turbulent transonic buffet on wide-span infinite wings,” *arXiv*, 2024, p. 2401.14793. URL <https://arxiv.org/abs/2406.01232>.
- [11] Giannelis, N. F., Vio, G. A., and Levinski, O., “A review of recent developments in the understanding of transonic shock buffet,” *Progress in Aerospace Sciences*, Vol. 92, No. May, 2017, pp. 39–84. <https://doi.org/10.1016/j.paerosci.2017.05.004>, URL <http://dx.doi.org/10.1016/j.paerosci.2017.05.004><http://linkinghub.elsevier.com/retrieve/pii/S0376042117300271>.
- [12] Crouch, J. D., Garbaruk, A., and Magidov, D., “Predicting the onset of flow unsteadiness based on global instability,” *Journal of Computational Physics*, Vol. 224, No. 2, 2007, pp. 924–940. <https://doi.org/10.1016/j.jcp.2006.10.035>.
- [13] Zauner, M., De Tullio, N., and Sandham, N. D., “Direct numerical simulations of transonic flow around an airfoil at moderate Reynolds numbers,” *AIAA Journal*, Vol. 57, No. 2, 2019, pp. 597–607. <https://doi.org/10.2514/1.J057335>.
- [14] Moise, P., Zauner, M., and Sandham, N. D., “Large-eddy simulations and modal reconstruction of laminar transonic buffet,” *Journal of Fluid Mechanics*, Vol. 944, 2022, p. A16. <https://doi.org/10.1017/jfm.2022.471>.
- [15] Placek, R., and Ruchała, P., “The flow separation development analysis in subsonic and transonic flow regime of the laminar airfoil,” *Transportation Research Procedia*, Vol. 29, 2018. <https://doi.org/10.1016/j.trpro.2018.02.029>, URL <http://linkinghub.elsevier.com/retrieve/pii/S2352146518300334><https://linkinghub.elsevier.com/retrieve/pii/S2352146518300334>.
- [16] Zauner, M., Moise, P., and Sandham, N. D., “On the Co-existence of Transonic Buffet and Separation-Bubble Modes for the OALT25 Laminar-Flow Wing Section,” *Flow, Turbulence and Combustion*, Vol. 110, No. 4, 2023. <https://doi.org/10.1007/s10494-023-00415-4>.
- [17] Moise, P., Zauner, M., Sandham, N. D., Timme, S., and He, W., “Transonic Buffet Characteristics Under Conditions of Free and Forced Transition,” *AIAA Journal*, Vol. 61, No. 3, 2023. <https://doi.org/10.2514/1.J062362>.
- [18] Brion, V., Dandois, J., Mayer, R., Reijasse, P., Lutz, T., and Jacquin, L., “Laminar buffet and flow control,” *Proceedings of the Institution of Mechanical Engineers, Part G: Journal of Aerospace Engineering*, 2019, p. 095441001882451. <https://doi.org/10.1177/0954410018824516>, URL <http://journals.sagepub.com/doi/10.1177/0954410018824516>.

- [19] Dandois, J., Mary, I., and Brion, V., “Large-eddy simulation of laminar transonic buffet,” *Journal of Fluid Mechanics*, Vol. 850, 2018, pp. 156–178. <https://doi.org/10.1017/jfm.2018.470>, URL https://www.cambridge.org/core/product/identifier/S0022112018004706/type/journal_article.
- [20] Jacquin, L., Molton, P., Deck, S., Maury, B., and Soulevant, D., “Experimental study of shock oscillation over a transonic supercritical profile,” *AIAA Journal*, Vol. 47, 2009, pp. 1985–1994.
- [21] Roos, F. W., “Some Features of the Unsteady Pressure Field in Transonic Airfoil Buffeting,” *Journal of Aircraft*, Vol. 17, No. 11, 1980, pp. 781–788. <https://doi.org/10.2514/3.57965>.
- [22] Lee, B. H. K., “Oscillatory shock motion caused by transonic shock boundary-layer interaction,” *AIAA Journal*, Vol. 28, No. 5, 1990, pp. 942–944. <https://doi.org/10.2514/3.25144>, URL <http://arc.aiaa.org/doi/10.2514/3.25144>.
- [23] Deck, S., “Numerical simulation of transonic buffet over an airfoil,” *AIAA journal*, Vol. 43, No. 7, 2005, pp. 1556–1566. <https://doi.org/10.2514/1.9885>.
- [24] Xiao, Q., Tsai, H.-M., and Liu, F., “Numerical Study of Transonic Buffet on a Supercritical Airfoil,” *AIAA Journal*, Vol. 44, No. 3, 2006, pp. 620–628. <https://doi.org/10.2514/1.16658>, URL <http://arc.aiaa.org/doi/10.2514/1.16658>.
- [25] Jacquin, L., Molton, P., Deck, S., Maury, B., and Soulevant, D., “An Experimental Study of Shock Oscillation over a Transonic Supercritical Profile,” *35th AIAA Fluid Dynamics Conference and Exhibit*, Vol. 47, American Institute of Aeronautics and Astronautics, Reston, Virigina, 2005, pp. 1985–1994. <https://doi.org/10.2514/6.2005-4902>, URL <https://arc.aiaa.org/doi/10.2514/1.30190http://arc.aiaa.org/doi/10.2514/6.2005-4902>.
- [26] Garnier, E., and Deck, S., “Large-eddy simulation of transonic buffet over a supercritical airfoil,” *Notes on Numerical Fluid Mechanics and Multidisciplinary Design*, Vol. 110, 2010, pp. 135–141. <https://doi.org/10.1007/978-3-642-14139-3-16>.
- [27] Robinson, G. M., and Keane, A. J., “Concise Orthogonal Representation of Supercritical Airfoils,” *Journal of Aircraft*, Vol. 38, No. 3, 2001, pp. 580–583. <https://doi.org/10.2514/2.2803>, URL <https://doi.org/10.2514/2.2803>.
- [28] Olson, E. D., *Three-Dimensional Piecewise-Continuous Class-Shape Transformation of Wings*, 2015. <https://doi.org/10.2514/6.2015-3238>, URL <https://arc.aiaa.org/doi/abs/10.2514/6.2015-3238>.
- [29] Karman, M., McNamara, M., and Coder, J. G., *Airfoil Optimization via the Class-Shape Transformation and Orthogonal Deformation Modes*, 2019. <https://doi.org/10.2514/6.2019-3173>, URL <https://arc.aiaa.org/doi/abs/10.2514/6.2019-3173>.
- [30] Sobieczky, H., *Parametric Airfoils and Wings*, 1998, pp. 71–88. https://doi.org/https://doi.org/10.1007/978-3-322-89952-1_4.
- [31] Sóbester, A., “Concise airfoil representation via case-based knowledge capture,” *AIAA Journal*, Vol. 47, No. 5, 2009, pp. 1209–1218. <https://doi.org/10.2514/1.40119>.
- [32] Masters, D. A., Taylory, N. J., Rendall, T. C., Allen, C. B., and Poole, D. J., “Review of aerofoil parameterisation methods for aerodynamic shape optimisation,” *53rd AIAA Aerospace Sciences Meeting*, , No. January, 2015. <https://doi.org/10.2514/6.2015-0761>.
- [33] Yao, Y., Shang, Z., Castagna, J., Sandham, N., Johnstone, R., Sandberg, R., Suponitsky, V., Redford, J., Jones, L., and De Tullio, N., “Re-Engineering a DNS Code for High-Performance Computation of Turbulent Flows,” *47th AIAA Aerospace Sciences Meeting including The New Horizons Forum and Aerospace Exposition*, American Institute of Aeronautics and Astronautics, Orlando, 2009. <https://doi.org/10.2514/6.2009-566>, URL <http://arc.aiaa.org/doi/10.2514/6.2009-566>.
- [34] Touber, E., and Sandham, N. D., “Large-eddy simulation of low-frequency unsteadiness in a turbulent shock-induced separation bubble,” *Theor. Comput. Fluid Dyn.*, Vol. 23, 2009, pp. 79–107. <https://doi.org/10.1007/s00162-009-0103-z>.
- [35] Sansica, A., Sandham, N. D., and Hu, Z., “Forced response of a laminar shock-induced separation bubble,” *Physics of Fluids*, Vol. 6, No. 093601, 2014.
- [36] Sansica, A., Sandham, N. D., and Hu, Z., “Instability and low-frequency unsteadiness in a shock-induced laminar separation bubble,” *Journal of Fluid Mechanics*, Vol. 798, 2016, pp. 5–26. <https://doi.org/10.1017/jfm.2016.297>, URL https://www.cambridge.org/core/product/identifier/S0022112016002974/type/journal_article.
- [37] Jones, L., Sandberg, R., and Sandham, N., “Direct numerical simulations of forced and unforced separation bubbles on an airfoil at incidence,” *Journal of Fluid Mechanics*, Vol. 602, 2008, pp. 175–207. <https://doi.org/10.1017/S0022112008000864>, URL <http://eprints.soton.ac.uk/55698/>.

- [38] De Tullio, N., and Sandham, N. D., “Direct numerical simulations and modal analysis of subsonic flow over swept airfoil sections,” 2019. URL <https://arxiv.org/abs/1901.04727>.
- [39] Zauner, M., “Direct numerical simulation and stability analysis of transonic flow around airfoils at moderate Reynolds numbers,” Ph.D. thesis, University of Southampton, 2019.
- [40] Zauner, M., and Sandham, N. D., “Wide domain simulations of flow over an unswept laminar wing section undergoing transonic buffet,” *Physical Review Fluids*, Vol. 5, No. 8, 2020. <https://doi.org/10.1103/PhysRevFluids.5.083903>.
- [41] Carpenter, M. H., Nordström, J., and Gottlieb, D., “A Stable and Conservative Interface Treatment of Arbitrary Spatial Accuracy,” *Journal of Computational Physics*, Vol. 148, No. 2, 1999, pp. 341–365. <https://doi.org/10.1006/jcph.1998.6114>, URL <http://linkinghub.elsevier.com/retrieve/pii/S0021999198961149>.
- [42] Sansica, A., “Stability and Unsteadiness of Transitional Shock-Wave/Boundary-Layer Interactions in Supersonic Flows,” *PhD Thesis, University of Southampton*, 2015, pp. 179–184. URL <https://eprints.soton.ac.uk/385891/>.
- [43] Sandberg, R. D., and Sandham, N. D., “Nonreflecting Zonal Characteristic Boundary Condition for Direct Numerical Simulation of Aerodynamic Sound,” *AIAA Journal*, Vol. 44, No. 2, 2006, pp. 402–405. <https://doi.org/10.2514/1.19169>, URL <http://arc.aiaa.org/doi/10.2514/1.19169>.
- [44] Sandhu, H., and Sandham, N., “Boundary conditions for spatially growing compressible shear layers,” Tech. rep., Faculty of Engineering, Queen Mary and Westfield College, University of London, 1994.
- [45] Zauner, M., and Sandham, N. D., “Modal Analysis of a Laminar-Flow Airfoil under Buffet Conditions at $Re = 500,000$,” *Flow, Turbulence and Combustion*, 2019. <https://doi.org/10.1007/s10494-019-00087-z>, URL <http://link.springer.com/10.1007/s10494-019-00087-z>.
- [46] Jacobs, C. T., Zauner, M., De Tullio, N., Jammy, S. P., Lusher, D. J., and Sandham, N. D., “An error indicator for finite difference methods using spectral techniques with application to aerofoil simulation,” *Computers & Fluids*, Vol. 168, 2018, pp. 67–72. <https://doi.org/10.1016/j.compfluid.2018.03.065>, URL <http://linkinghub.elsevier.com/retrieve/pii/S0045793018301695>.
- [47] Visbal, M. R., and Gaitonde, D. V., “On the Use of Higher-Order Finite-Difference Schemes on Curvilinear and Deforming Meshes,” *Journal of Computational Physics*, Vol. 181, No. 1, 2002, pp. 155–185. <https://doi.org/10.1006/jcph.2002.7117>, URL <http://linkinghub.elsevier.com/retrieve/pii/S0021999102971172>.
- [48] Zauner, M., and Sandham, N. D., “LES study of the three-dimensional behaviour of unswept wing sections at buffet conditions,” *Direct and Large-Eddy Simulation XII*, 2019.
- [49] Lusher, D. J., Jammy, S. P., and Sandham, N. D., “Shock-wave/boundary-layer interactions in the automatic source-code generation framework OpenSBLI,” *Computers & Fluids*, Vol. 173, 2018, pp. 17 – 21.
- [50] Lusher, D. J., Jammy, S. P., and Sandham, N. D., “OpenSBLI: Automated code-generation for heterogeneous computing architectures applied to compressible fluid dynamics on structured grids,” *Computer Physics Communications*, Vol. 267, 2021, p. 108063. <https://doi.org/https://doi.org/10.1016/j.cpc.2021.108063>.
- [51] Reguly, I. Z., Mudalige, G. R., Giles, M. B., Curran, D., and McIntosh-Smith, S., “The OPS Domain Specific Abstraction for Multi-block Structured Grid Computations,” IEEE Press, 2014, pp. 58–67.
- [52] Chapelier, J.-B., Lusher, D. J., Van Noordt, W., Wenzel, C., Gibis, T., Mossier, P., Beck, A., Lodato, G., Brehm, C., Ruggeri, M., Scalo, C., and Sandham, N., “Comparison of high-order numerical methodologies for the simulation of the supersonic Taylor–Green vortex flow,” *Physics of Fluids*, Vol. 36, No. 5, 2024, p. 055146. <https://doi.org/10.1063/5.0206359>, URL <https://doi.org/10.1063/5.0206359>.
- [53] Coppola, G., Capuano, F., Pirozzoli, S., and de Luca, L., “Numerically stable formulations of convective terms for turbulent compressible flows,” *Journal of Computational Physics*, Vol. 382, 2019, pp. 86–104.
- [54] Yee, H. C., and Sjögren, B., “Recent developments in accuracy and stability improvement of nonlinear filter methods for DNS and LES of compressible flows,” *Computers & Fluids*, Vol. 169, 2018, pp. 331–348.
- [55] Bogey, C., and Bailly, C., “A family of low dispersive and low dissipative explicit schemes for flow and noise computations,” *Journal of Computational Physics*, Vol. 194, No. 1, 2004, pp. 194–214. <https://doi.org/https://doi.org/10.1016/j.jcp.2003.09.003>.
- [56] Lusher, D. J., Zauner, M., Sansica, A., and Hashimoto, A., “Automatic Code-Generation to Enable High-Fidelity Simulations of Multi-Block Airfoils on GPUs,” *AIAA Scitech 2023 Forum, AIAA SciTech Forum*, 2023.

- [57] Lusher, D. J., Sansica, A., and Hashimoto, A., “Effect of Tripping and Domain-Width on Transonic Buffet on Periodic NASA-CRM Airfoils,” *AIAA Journal*, *Accepted*, 2024, p. 2401.14793. URL <https://arxiv.org/abs/2401.14793>.
- [58] Hashimoto, A., Murakami, K., Aoyama, T., Ishiko, K., Hishida, M., Sakashita, M., and Lahur, P., “Toward the Fastest Unstructured CFD Code ‘FaSTAR’,” *50th AIAA Aerospace Sciences Meeting including the New Horizons Forum and Aerospace Exposition*, , No. AIAA 2012-1075, 2012. <https://doi.org/10.2514/6.2012-1075>.
- [59] Lusher, D. J., Sansica, A., Sandham, N. D., Meng, J., Siklósi, B., and Hashimoto, A., “OpenSBLI v3.0: High-Fidelity Multi-Block Transonic Aerofoil CFD Simulations using Domain Specific Languages on GPUs,” *Computer Physics Communications*, *Under Review*, 2024.
- [60] Zauner, M., and Sandham, N. D., “PolyGridWizZ Beta-version 0.0.1,” 2018. <https://doi.org/10.5281/ZENODO.1245598>, URL <https://doi.org/10.5281/zenodo.1245598#.WvWOYdDobmF.mendeley>.
- [61] Zauner, M., and Sandham, N. D., “Multiblock structured grids for direct numerical simulations of transonic wing sections,” *ICCFD Conference*, Barcelona, 2018.
- [62] Zauner, M., Jacobs, C. T., and Sandham, N. D., “Grid refinement using spectral error indicators with application to airfoil DNS,” *ECCM-ECFD Conference*, Glasgow, 2018. URL <http://www.eccm-ecfd2018.org/frontal/docs/Ebook-Glasgow-2018-ECCM-VI-ECFD-VII.pdf>.
- [63] Zauner, M., Sandham, N. D., Wheeler, A. P. S., and Sandberg, R. D., “Linear Stability Prediction of Vortex Structures on High Pressure Turbine Blades,” *International Journal of Propulsion and Power*, Vol. 2, No. 8, 2017. <https://doi.org/10.3390/ijtpp2020008>.
- [64] Zauner, M., and Sandham, N. D., “Incipient buffet over laminar-flow airfoil - A DNS study at moderate Reynolds numbers,” *ETTM12 proceedings*, 2018.